



### Science Arts & Métiers (SAM)

is an open access repository that collects the work of Arts et Métiers Institute of Technology researchers and makes it freely available over the web where possible.

This is an author-deposited version published in: <https://sam.ensam.eu>  
Handle ID: <http://hdl.handle.net/10985/17875>

#### To cite this version :

Saptarshee MITRA, Mohamed EL MANSORI, Antonio RODRÍGUEZ DE CASTRO, Marius COSTIN - Study of the evolution of transport properties induced by additive processing sand mold using X-ray computed tomography - Journal of Materials Processing Technology - Vol. 277, p.116495 - 2020

Any correspondence concerning this service should be sent to the repository

Administrator : [archiveouverte@ensam.eu](mailto:archiveouverte@ensam.eu)



1 **Study of the evolution of transport properties induced by additive processing sand mold**  
2 **using X-ray computed tomography**

3

4 Saptarshree Mitra<sup>1</sup>, Mohamed EL Mansori<sup>1,2</sup>, Antonio Rodríguez de Castro<sup>3</sup>, Marius Costin<sup>4</sup>

5

6 <sup>1</sup>*Laboratoire MSMP – EA7350, Arts et Métiers ParisTech, 2 Cours des Arts et Métiers, 13617*  
7 *Aix-en-Provence, France*

8 <sup>2</sup>*Texas A&M Engineering Experiment Station, College Station, TX 77843, USA*

9 <sup>3</sup>*Laboratoire MSMP – EA7350, Arts et Métiers ParisTech, Rue Saint Dominique, 51006*  
10 *Châlons-en-Champagne, France*

11 <sup>4</sup>*CEA, LIST, Department of Imaging & Simulation for Non-Destructive Testing, F-91191 Gif-*  
12 *sur-Yvette, France*

13

14

15

16

17

18

19

20

21

## 22 **Abstract**

23 Accurate characterization of the mass transport properties of additively processed sand molds  
24 is essential in order to achieve reproducibility of the produced castings and control of gas  
25 defects in foundry industries. The present work highlights the potential use of X-ray micro-  
26 computed tomography ( $\mu$ -CT) to characterize the evolution of permeability and some major  
27 microstructural features of such additively processed sand molds. The evolution of mass  
28 transport properties of sand mold samples under specific processing conditions met in  
29 additive manufacturing and its influence on the porosity, the permeability, the tortuosity, and  
30 the pore and throat size distributions were characterized from 3D images provided by X-Ray  
31  $\mu$ -CT. The obtained results showed that the mass transport properties of additively processed  
32 sand molds can be closely predicted by using non-destructive in situ methods, such that  
33 improvements to the casting can be made to create more optimized 3D printed structures for  
34 foundry applications.

35

36 **Keywords:** Additive manufacturing; 3D-printed casting sand mold; Permeability; Pore Size  
37 Distribution; X-ray  $\mu$ -CT; Numerical simulations; Pore network modeling.

38

## 39 **1. Introduction**

40

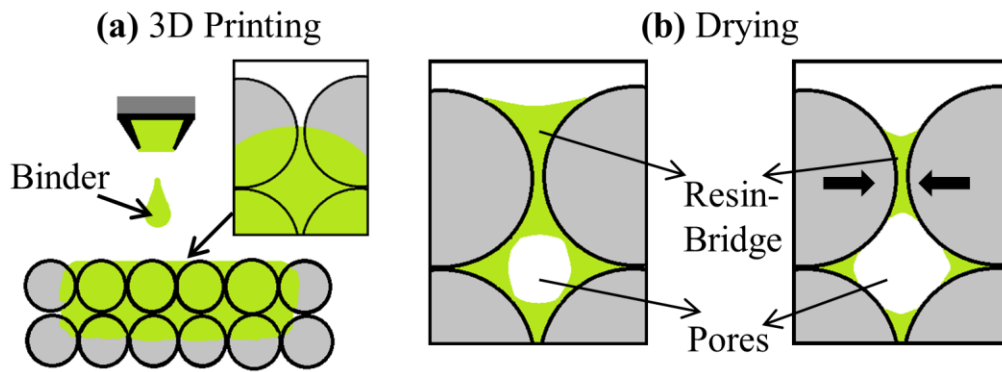
41 Three-Dimensional Printing (3DP) technology, also termed as Additive Processing (AP) or  
42 joining technology, emerged as a new rapid manufacturing method in foundry industries to  
43 build three-dimensional (3D) sand molds directly from Computer-Aided Design (CAD)  
44 models in layers. As compared with the traditional conventional sand mold, (Sachs et al.,  
45 1990) stated that this kind of rapid-prototyping technique offers the ability to efficiently

46 manufacture sand molds and cores in casting industry with optimized geometries as designed  
47 with CAD without the need of extensive molding. Additively processed sand mold is also  
48 advantageous over conventional methods due to its ability to reduce surface defects in the  
49 molds as shown by (Hawaldar and Zhang, 2018). Rapid prototyping technique has been  
50 accepted extensively in the casting industries due to its proven capability to reproduce a  
51 virtually complex designed object into a real casting mold. (Almaghariz, 2015) studied the  
52 economic advantage of 3DP technology and found that there is no influence of part  
53 complexity on the manufacturing costs of molds and cores. This technique allows the  
54 production of highly complex components in a cost-effective way as shown by (Almaghariz et  
55 al., 2016) and good surface finish as shown by (Hawaldar and Zhang, 2018). Despite being  
56 still limited in number, the applications of AP technique are much diversified, including  
57 aerospace, automobile, and medical industries. Consequently, 3DP represents a step forward  
58 towards autonomous casting in which a sand mold can be printed without any machining  
59 stage. In this regard, (Upadhyay et al., 2017) published an extensive literature review  
60 elsewhere, so only the key features of additively processed sand molds are reminded in the  
61 present article.

62

63 AP has enabled the casting industries and foundries to produce more complex sand molds  
64 without using any kind of physical model, through a succession of thin layer which are  
65 directly generated from 3D CAD files. The layer-based rapid prototyping technology, or  
66 Powder Binder Jetting (PBJ), consists in bonding individual particles with a liquid resin  
67 binder, which generates porous parts. The existence of such porosity is necessary in casting  
68 sand molds so that the gases can be efficiently evacuated from the mold cavity through the  
69 interstices during filling of the mold. This minimizes the risk of casting defects caused by gas  
70 trapping in the liquid alloy. Fig. 1(a) describes the PBJ process, in which ceramics kind of

71 materials are generally used as to provide refractoriness to the mold, and a liquid resin binder  
72 provides cohesion in between such ceramic particles by forming capillary bridges, Fig. 1(b).  
73 For metal casting, a temperature-resistant material is required, so silica sand is generally used  
74 as granular material for the PBJ process, and a furan resin is commonly taken as a liquid  
75 binder due its high performance in terms of dimensional accuracy and mechanical strength of  
76 the printed mold. Also, various 3D printing process parameters directly affect the quality of  
77 the sand mold. In particular, the relationship between the printing process parameters (print  
78 position/orientation in job-box, recoater speed, and print resolution) and their influence on the  
79 properties of the 3DP sand mold have been extensively investigated in previous works using  
80 both mathematical modelling by (Coniglio et al., 2017) and experimental validations by  
81 (Sivarupan et al., 2017). (Sivarupan et al., 2017) showed how the printing processing  
82 parameters affected mechanical properties in 3DP sand mold. It was also reported by (Mitra et  
83 al., 2019) that the mechanical strength and permeability of 3DP sand molds are deeply  
84 dependent on the amount of binder and the ageing conditions. In this regard, the evolution of  
85 permeability and mechanical strength of such additively processed silica sand molds during  
86 curing was studied in a recent work by (Mitra et al., 2018) for different binder contents and  
87 curing parameters, showing that the 3D printed sand molds could be stored for long time at  
88 room temperature before being used for metal casting, while no substantial variation in  
89 strength of 3DP mold was observed below 100 °C, the gas permeability was found to decrease  
90 with increase in curing temperature. However it is of equal importance for morphological  
91 characterization of such additively processed porous structures to be standardized in foundry  
92 with proven quality control, especially as the 3DP structures can be customized and changed  
93 (based on printing process parameters) easily to alter its mass transport properties based on  
94 casting requirements.



95

96 **Fig. 1.** The PBJ process showing, (a) the initial distribution of furan binder within the silica  
 97 sand particles, (b) the drying stage of resin-bridges by infrared heating during the printing of  
 98 the mold and the optional curing stage to obtain stronger resin-bridge after printing of the  
 99 mold.

100

101 Characterization of mass transport properties through pore networks with complex geometry  
 102 and connectivity, such as 3DP sand molds, is essential in order to assess the risks of  
 103 incomplete filling and gas porosity in castings. The fundamental microstructural  
 104 characteristics include grain size distribution, pore size distribution, throat (pore constriction)  
 105 size distribution, pore-to-throat size ratio, pore connectivity, and tortuosity. These  
 106 microscopic physical properties will control the macroscopic characteristics of the 3DP molds  
 107 in terms of permeability and porosity governing the flow of liquid metal, and, more generally,  
 108 the heat and mass transport within the 3DP sand mold. Therefore, knowledge of the  
 109 relationships of 3DP process parameters and these microscopic characteristics is of vital  
 110 importance to predict casting defects. On this subject, it was stated earlier by (Sivarupan et al.,  
 111 2017) that high recoater speeds lead to lower grain packing densities in 3DP molds (porosity  
 112 depends on recoating speed). It is also known that high levels of sand compaction reduce  
 113 permeability due to the decrease in volume available for fluid flow and the increase in specific  
 114 surface of the interstices. Pore Network Modelling (PNM) offers a simple demonstration of

115 the complex pore structure and topology, but quiet more accurate than traditional bundle-of-  
116 capillaries model. In PNM the void phase is divided into a set of spherical pores connected by  
117 cylindrical throats. A complete review of PNM for porous geometries (pore network  
118 construction) has been studied elsewhere by (Xiong et al., 2016). (Huang et al., 2019) used  
119 PNM to extract the network of pores and the connected throats from a fibrous material to  
120 simulate two-phase flow. It was shown by (Degruyter et al., 2009) and (Degruyter et al.,  
121 2010) that the permeability can be predicted using the throat size distributions with the  
122 modified Archie's law.

123

124 In the industrial foundry processes, numerical simulations of mold filling and casting  
125 solidification are employed in order to optimize the part designs, reduce the manufacturing  
126 costs and prevent defect generation. However, the lack of accurate estimations of key inputs,  
127 e.g., local porosity, density, permeability, and strength, limits the usefulness of the obtained  
128 numerical results. Therefore, it is crucial to develop a non-destructive method to properly  
129 characterize 3DP sand molds in order to predict the relationships between process parameters  
130 and the inputs to such simulations. Other non-destructive methods include the traditional  
131 permeability test in which air is injected to the 3D printed sample (although they need  
132 sampling of the mold). Also, Scanning Electron Microscope (SEM) imaging could be  
133 considered as a suitable non-destructive method, but only 2D microstructural information can  
134 be extracted. Although Mercury Intrusion Porosimetry (MIP) is by far the most popular  
135 method for characterizing the pore size distribution of porous materials with pores in the  
136 range of 500  $\mu\text{m}$  to 3.5 nm as stated by (Giesche, 2006), MIP experiments are not expected to  
137 work well on unconsolidated materials like 3D printed casting sands because the applied  
138 pressure damages the material and its void-structure. X-ray micro computed tomography ( $\mu$ -  
139 CT) is a non-destructive and non-intrusive method as stated by (FLANNERY et al., 1987),

140 allowing the characterization of 3D printed sand mold specimens. On this regard, a complete  
141 review of X-ray  $\mu$ -CT and its applications has been studied elsewhere by (De Chiffre et al.,  
142 2014). X-ray  $\mu$ -CT has emerged as a powerful nondestructive technique (NDT) for the direct  
143 3D characterization of complex porous geometries. (Hazlett, 1995) stated that the 3D images  
144 of the pore space, like those provided by X-ray  $\mu$ -CT, can be used for direct computation of  
145 multiphase fluid flow and to reliably characterize permeability from the realistic digital  
146 images provided by this technique.

147

148 Different numerical methods exist for the simulation of creeping flow through porous media  
149 at the microscale, e.g., Finite Volume Method (FVM) and Lattice Boltzmann Method (LBM).  
150 (Jaganathan et al., 2008) used FVM to model fluid flow through the real microstructure of a  
151 fibrous mat to predict the permeability and compared them to various analytical expressions.  
152 (Soulaine, 2015) used FVM to perform a direct numerical simulation of fluid flow in a fully  
153 saturated porous media for the prediction of permeability from  $\mu$ -CT image. (Thabet and  
154 Straatman, 2018) idealized a geometrical introduced to characterize small volume of packed  
155 sand in pore-level computations using YADE (Yet Another Development Engine) solver. In  
156 previous research by (Boek and Venturoli, 2010), it was proved that using LBM, to obtain  
157 permeability from a digital image is a reliable alternative to destructive traditional  
158 measurements. (Malaspinas et al., 2010) presented a novel lattice Boltzmann scheme to  
159 simulate viscoelastic fluid flows, and stated that LBM results were found to be in good  
160 agreement with analytical and other numerical results. In this sense, some works were  
161 performed earlier by (Degruyter et al., 2010) combining LBM and X-ray  $\mu$ -CT for the  
162 calculation of permeability of volcanic pumices. (Kadawu, 2014) characterized the local  
163 density of sand mold using industrial computed tomography, and found good agreement with  
164 the experimental density of sand mold. Some typical results were reported recently by



165 (Sivarupan et al., 2018) for the use of X-ray  $\mu$ -CT to characterize the additively processed  
166 porous structure like 3DP sand mold. (Anbar et al., 2019) used LBM to predict permeability  
167 from a computer-generated sphere packing, and to study the impact of sand compaction from  
168 the simulations. However, no other literature review exists tackling the particular case of  
169 permeability characterization of 3DP sand molds from  $\mu$ -CT digital images using LBM and  
170 PNM.

171

172 The current work will describe an accurate and rigorous method to characterize the physical  
173 properties of such additively processed sand mold from the digital images provided by X-ray  
174  $\mu$ -CT. The first point of inquiry is, what is the real local permeability of 3D printed structure?  
175 To achieve that goal, a set of X-ray  $\mu$ -CT experiments are first performed on additively  
176 processed silica samples with different silica grain sizes and binder percentage. The  
177 microstructural properties are secondly determined through the use of image analysis  
178 techniques and PNM. Then, LBM numerical simulations and analytical methods are used to  
179 predict the permeability of the samples, and the results are subsequently compared to  
180 experimental measurements provided by traditional techniques.

181

## 182 **2. Materials and methods**

183

### 184 ***2.1. Manufacturing process of 3DP sand mold specimen***

185

186 The raw materials in the current experiments were silica sand and a furfuryl-alcohol-  
187 composed binder (furan resin binder) with a density of (1.1-1.2) g/cm<sup>3</sup>, as provided by

188 (ExOne, 2014). The silica sand particles used in the present experiments had a mean particle  
189 diameter of 140  $\mu\text{m}$  and 190  $\mu\text{m}$  as specified by the supplier in (ExOne, 2013).

190

191 The samples were designed with NetFabb<sup>TM</sup> software and subsequently converted to .stl  
192 format. The designed samples were printed with an ExOne S-Print-Furan 3D printing  
193 machine, over a job-box size of  $800 \times 500 \times 400 \text{ mm}^3$ . The process of 3D printing began by  
194 adding sulfonic acid (0.18 wt% of the sand) with 8 kg of sand inside a mixing chamber. The  
195 acid-activated sand mixture was then transferred to the re-coater. Successive layers of sand  
196 grains were added and compacted over the build platform by means of a re-coater head.  
197 Furfuryl alcohol binder was then gradually injected by the print head nozzle on top of these  
198 compacted sand layer beds in order to bind them. The injected furan-resin-binder droplets  
199 tend to form a coating layer over individual sand grains. This causes the resin-bonded sand  
200 grains to crosslink with each other by forming a resin bridge between the sand grains. The  
201 additive processing of resin-bonded sand in layers continued until the designed part is  
202 fabricated. This resin bridge in between the sand particles hardens gradually, hence providing  
203 strength to the printed mold.

204

205 For the X-ray CT analysis, 10 small-grain and 10 big-grain cylindrical samples with different  
206 binder percentages were printed and named accordingly as provided in Table 1. A set of 20 (5  
207  $\times$  2 different binder content  $\times$  2 different grain size) cylindrical specimens were printed for  
208 the experimental permeability measurements, with a diameter of 50 mm and height of 50 mm.

209

210

211

212

**Table 1.** 3DP specimens used for analysis

Sample	Binder content (wt%)	Average grain size ( $\mu\text{m}$ )
Small Grains with High Binder content (SGHB)	~2	140
Small Grains with Low Binder content (SGLB)	~1	140
Big Grains with High Binder content (BGHB)	~2	190
Big Grains with Low Binder content (BGLB)	~1	190

213

214 The choice of the binder percentages was based on the recommended values for binder  
 215 contents (0.9% - 2%) reported in previous research by (Hawaladar and Zhang, 2018). The  
 216 dimensions of the 3D printed parts for X-ray  $\mu$ -CT tests were measured manually using  
 217 Vernier caliper, with top height of  $12 \pm 0.02$  mm, base height of  $10 \pm 0.02$  mm, top diameter  
 218 of  $4 \pm 0.02$  mm and base diameter of  $6 \pm 0.02$  mm, respectively (the uncertainty corresponds  
 219 to 95% confidence interval), Fig. 2(d). The temperature of the 3D printing room was  
 220 controlled at  $25 \pm 2$  °C and the measured relative humidity of the room was  $40 \pm 10\%$ . A  
 221 detailed experimental investigation of the effects of mass transport improvement on  
 222 mechanical strength of 3DP sand mold was presented in previous works by (Mitra et al.,  
 223 2018), (Mitra et al., 2019) and (Ramezani Dana and El Mansori, 2019).

224

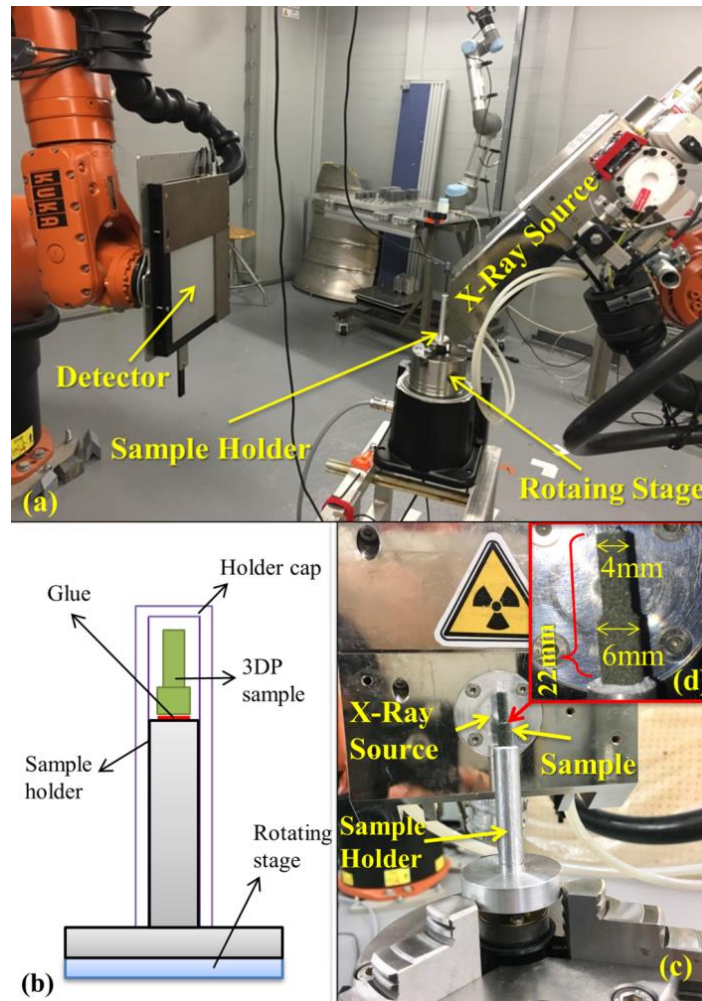
## 225 ***2.2. Volumetric reconstruction of 3DP mold via X-ray tomography***

226

### 227 **2.2.1. X-ray micro computed tomography: image acquisition and post-processing**

228

229 In the present study, reconstructed 3D tomographic images of 3DP specimens were used to  
230 extract information on microstructural characteristics (grains, pores, porosity, tortuosity) and  
231 permeability through image analysis, PNM and LBM simulations. The X-ray  $\mu$ -CT images  
232 were obtained at a facility of CEA LIST (NDT department). The X-ray equipment consists of  
233 a micro-focus X-ray generator, a flat panel detector, and a turn-table, situated in a large  
234 inspection cell which enables the addition of instrumentation for in-situ characterizations. The  
235 X-ray generator is a Viscom 225 kV (320 W) model with a micro-focus spot-size. The  
236 detector is a Perkin Elmer XRD0822 model having 1024 x 1024 pixels of 200x200  $\mu\text{m}^2$  in  
237 size, and the acquisitions were performed in a classical setup with a rotating sample ( $360^\circ$ )  
238 and static source and detector positions. The optimum scan settings for the specimens were  
239 determined, obtaining 100 kVp, 60  $\mu\text{A}$ , and 1 second exposure time. For each CT scan, a  
240 number of 900 projections were acquired, with an integration time of 1 second. The total  
241 acquisition scan was about 30 minutes. The scan facility uses a temperature controlled  
242 inspection cell and therefore the impact of temperature variations is considered negligible.  
243 The magnification factor was set to 40, which gives a voxel size of 5  $\mu\text{m}^3$  in the CT images.  
244 The reconstructions and preliminary analysis were performed by using VGSTUDIO MAX<sup>TM</sup>  
245 commercial software at a facility of CEA LIST (NDT department). The setup is shown in Fig.  
246 2 as well as the sample holder and the details of specimens.



247

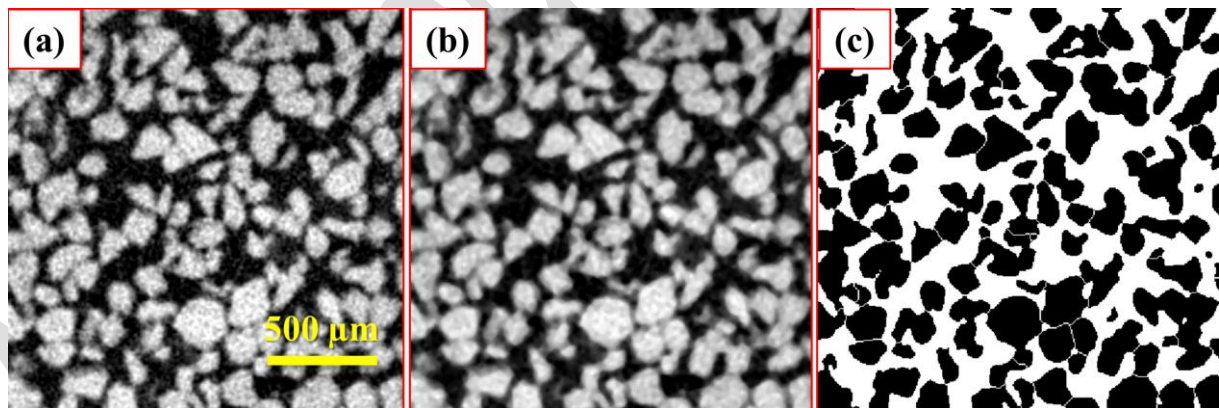
248 **Fig. 2.** Different views and schemes of the experimental X-ray  $\mu$ -CT setup showing: (a) the  
 249 robotic X-ray inspection platform, (b) a schematic design of the sample holder (c) the sample  
 250 holder and (d) a zoom-in view including the dimensions of the sample.

251

252 For the morphological assessment of 3DP sand mold, the acquired 3D images were binarized  
 253 and analyzed using the default algorithms provided by (Schindelin et al., 2012) included in  
 254 ImageJ and subsequently post-treated using different software: ParaView by (Ayachit  
 255 Utkarsh, 2015), PALABOS by (Latt J, 2009) and OPENPNM by (Gostick et al., 2016). The  
 256 post-treatment procedure starts by cropping and scaling the raw stack of images, resulting in  
 257 the cross-sectional dimensions displayed in Fig. 3. Reconstructed X-ray  $\mu$ -CT images were  
 258 then filtered using a variance weighted mean filter to reduce the effect of background noise. A

259 median filter of 2 voxels was applied, as shown in Fig. 3(b), to reduce noise without merging  
260 the solid particles. The cropped image was then binarized using the Otsu algorithm by (Smith  
261 et al., 2010) and was converted into an 8-bit greyscale thresholded image, as shown in Fig.  
262 3(c). The reconstructed pixel data were then converted into an 8-bit grayscale image. It should  
263 be noted that a 3DP specimen consists of three phases with different attenuation coefficients:  
264 silica sand, resin binder and air (pores). It is to be noted that the binder produces a low  
265 contrast with respect to silica and is difficult to isolate in a CT image. Therefore, only two  
266 phases, e.g. void and solid, were identified in the present experiments. However, the absence  
267 of binder in the segmented image is not expected to significantly alter the computed  
268 permeability values, due to the low binder contents (1 – 2 wt%) and based on previous results  
269 as shown by (Mitra et al., 2019). Furthermore, the thresholding of the CT data was carried out  
270 in an iterative manner and validation of the threshold was performed through comparison of  
271 the estimated porosity to the porosity measured with a classical mass weighting apparatus.

272



273

274 **Fig. 3.** Steps during post-treatment of the acquired images: (a) raw image (2D slice), (b)  
275 median filter treatment and (c) converted to 8-bit greyscale binary image. White represents  
276 interstices and black corresponds to solid grains in the binary image.

277

278 **2.2.2. Grain size distribution and measurement of tortuosity**

279

280 The sand grain shape and size plays an important role in the fabrication of 3DP sand mold, as  
281 they deeply impact the permeability of the sand molds, hence casting quality. The finer the  
282 silica grains, lower the permeability will be, similarly the coarse silica grains will lead to a  
283 higher permeability. Grains are generally categorized based on their shapes; rounded, sub-  
284 angular and angular. Rounded grains lead to high permeability of sand mold, due to least  
285 contact with other grains during the sand compaction. However, these kinds of grain shape do  
286 not pack up to its maximum, hence lacks strength. Whereas sub-angular grains have low  
287 permeability with high strength values compared to the rounded grains. The angular grain  
288 provides higher strength to the 3DP mold, but with low permeability due to tight packing of  
289 grains. Therefore it was of great importance to characterize the grain size distribution along  
290 with their forms, as it directly affects the casting quality.

291

292 For the analysis of the silica grains size distribution, Morpholib - Distance Transform  
293 Watershed 3D algorithm by (Legland et al., 2016) included in ImageJ was applied to the  
294 thresholded images in order to separate touching objects (creating a border far from the center  
295 of the overlapping object). The watershed segmentation algorithm detects and separates pore  
296 bodies in 2D or 3D images. Then, the connected components are scrutinized using Analysis  
297 3D – Labelling plugin by (Boulos et al., 2013) from ImageJ. By using this algorithm, a new  
298 volume was generated in which all the particles were labeled. From the generated results, the  
299 equivalent diameter of each silica grain  $d_g$  was calculated using Eq. 1:

$$d_g = \sqrt[3]{6 \times \text{volmarch} / \pi} \quad (1)$$

300

301 with *volmarch* being the volume in marching cubes. Then, a result file in .xl format was  
302 generated by using the Analysis 3D – Parameter plugin by (Boulos et al., 2013) listing several  
303 parameters: volume in pixel, volume in marching cubes, surface with marching cubes. A  
304 Granulometry-histogram plot was plotted using the total number of labeled particles as a  
305 function of particle diameter as obtained from Eq. 1. Then, the sphericity of the particles was  
306 computed using the following formula (nearly-spherical shapes approaching value 1):

$$\text{sphericity} = 6 \times \text{volmarch} \times \sqrt{\pi / \text{surfacemarch}^3} \quad (2)$$

308  
309 Where *surfacemarch* is the surface with marching cubes as shown by (Boulos et al., 2013).  
310 Furthermore, the porosity of the 3DP specimen was calculated by dividing summation of  
311 resulting *volmarch* values by the size of the reconstructed image multiplied by total number  
312 of slices. Also, standard Kozeny–Carman equation (bundle of cylindrical capillaries model)  
313 was used to calculate permeability *k* from the obtained average grain diameter and pore space  
314 volume from the characterized  $\mu$ -CT images by:

$$k = \frac{\varepsilon_{bed}^3 d_s^2}{180(1 - \varepsilon_{bed})^2} \quad (3)$$

316  
317 where  $\varepsilon_{bed}$  is the average porosity of the  $\mu$ -CT images of the 3DP specimen and  $d_s$  is the  
318 average diameter of the silica grains.

319



320 To go further, the pore connectivity  $Z$  and the geometric tortuosity  $\tau$  of the 3D printed sand  
 321 mold specimens was also computed through an iterative-thinning algorithm (Median axis  
 322 algorithm) by using Skeletonize 3D and Analyze Skeleton plugins from ImageJ by (Ignacio  
 323 Arganda-Carreras et al., 2010) for all the 3DP specimens (SGLB, SGHB, BGLB, and BGHB).  
 324 The number of branches that originate from a junction (3, 4 and  $>4$  branches) is termed as  
 325 pore connectivity, and the ratio between the regular and the Euclidean length of such branches  
 326 is termed as geometric tortuosity. A result window from the plugin displays the node-to-node  
 327 distances ( $d_i$ ), Euclidian distances ( $d_{euclid}$ ), total number of junctions ( $n_j$ ), total number of  
 328 triple-branch junctions ( $n_t$ ), total number of quadruple-branch junctions ( $n_q$ ). Any junctions  
 329 above that is a high-order junctions ( $n_x$ ). It was shown earlier by (Hormann et al., 2016), that  
 330 the pore connectivity ( $Z$ ) can be calculated from ( $n_j$ ), ( $n_t$ ), ( $n_q$ ), and ( $n_x$ ), using Eq. 4 and  
 331 Eq. 5:

$$Z = 3 \frac{n_t}{n_j} + 4 \frac{n_q}{n_j} + 5 \frac{n_x}{n_j} \quad (4)$$

$$\frac{n_x}{n_j} = 1 - \frac{n_t}{n_j} - \frac{n_q}{n_j} \quad (5)$$

332 Where,  $n_t/n_j$ ,  $n_q/n_j$ , and  $n_x/n_j$  provides the fraction of nodes connecting 3, 4 and  $>4$   
 333 branches respectively.

334 And the tortuosity was calculated as being the average ratio between node-to-node network  
 335 distances ( $d_i$ ) and Euclidean distances ( $d_{euclid}$ ) as shown by (Ignacio Arganda-Carreras et al.,  
 336 2010) and (Hormann et al., 2016):

337

$$\tau = \frac{1}{n} \sum_{i=1}^n \frac{d_i}{d_{euclid}} \quad (6)$$

338 The results in terms of pore connectivity ( $Z$ ) and tortuosity ( $\tau$ ) are provided in Table 2. It can  
 339 be observed that most junctions have 3 branches, a significant number of junctions have 4  
 340 branches and only a few present 5 or more branches. An average pore connectivity value of  $Z$   
 341  $\approx 3$  is obtained. In this regard, (Sivarupan et al., 2018) showed in a previous work that the  
 342 speed at which the recoater spreads the sand particles on the job box platform affects the pore-  
 343 connectivity, hence affecting the permeability. It can be deduced from the results displayed in  
 344 Table 2 that the size of the grain does not affect pore connectivity, in contrast to the case of  
 345 recoating speed.

346 **Table 2.** Results from median axis algorithm, showing the pore connectivity and tortuosity

Sample	$n_t/n_j$	$n_q/n_j$	$n_x/n_j$	Pore connectivity ( $Z$ )	Tortuosity ( $\tau$ )
SGHB	0.721	0.211	0.067	3.346	1.223
SGLB	0.703	0.243	0.052	3.348	1.221
BGHB	0.833	0.131	0.034	3.201	1.218
BGLB	0.773	0.176	0.049	3.275	1.225

347

### 348 *2.3. Computational simulation of fluid flow in 3DP sand mold using Lattice Boltzmann*

#### 349 *Method*

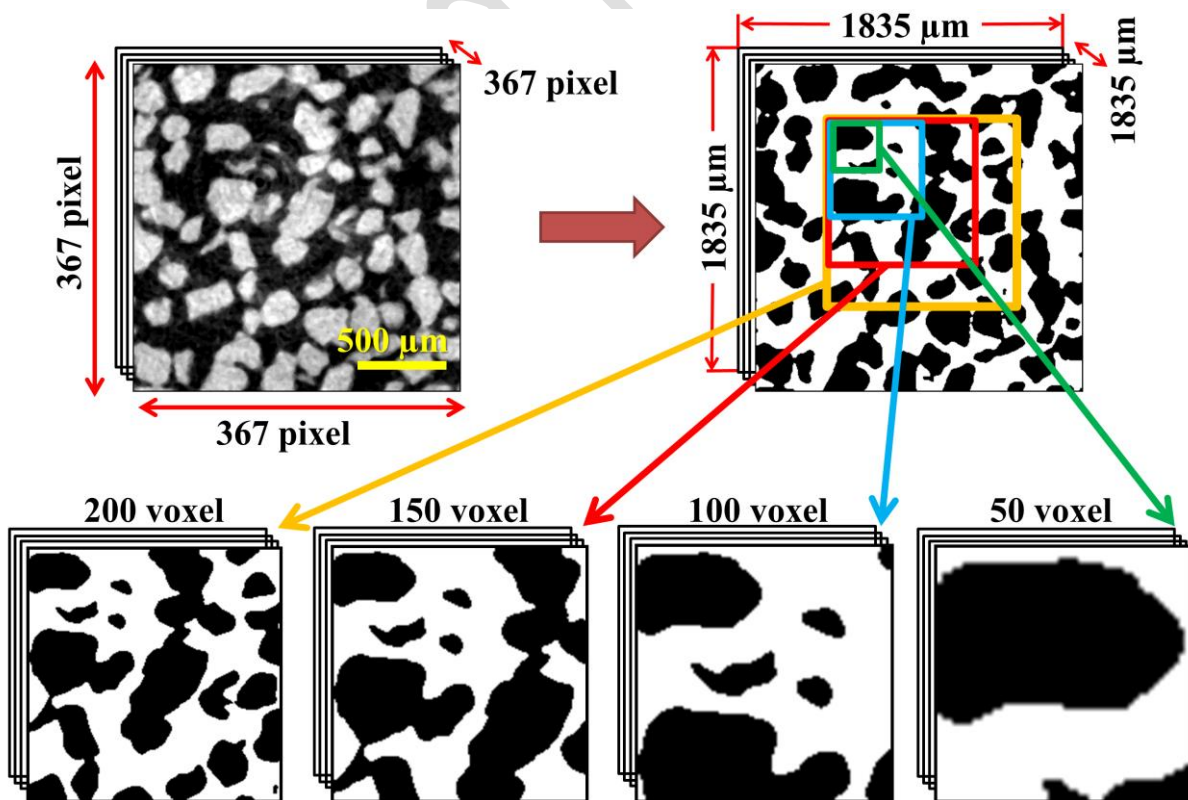
350

351 A volume of  $367 \times 367 \times 367$  voxel (corresponding to  $1835 \times 1835 \times 1835 \mu\text{m}^3$ ) was cropped  
 352 from the original reconstructed image with voxels of  $5^3 \mu\text{m}^3$ . The cropped image was then  
 353 binarized using the procedure presented in subsection 2.2.1. The porosity was then computed  
 354 by dividing the number of pore space voxels (white) by the total volume of the image stack.

355

356 The volume of the image being used as input to numerical simulations must be large enough  
357 to produce a representative and statistically meaningful value of permeability for the 3DP  
358 sand mold. While too big volumes would require a powerful and parallel computer clusters,  
359 the Representative Volume Element (RVE) must lead to statistically meaningful results while  
360 reducing computation time. Therefore, four different sizes of representative were selected  
361 from the original cropped binary image: 200×200×200 voxel, 150×150×150 voxels  
362 100×100×100 voxels and 50×50×50 voxels, as shown in Fig. 4, corresponding to  
363 1000×1000×1000  $\mu\text{m}^3$ , 750×750×750  $\mu\text{m}^3$ , 500×500×500  $\mu\text{m}^3$ , and 250×250×250  $\mu\text{m}^3$   
364 volumes, respectively. These 4 cropped segmented stacks were then used as inputs to the  
365 LBM numerical simulations performed with Lattice-Boltzmann Method (LBM) solver  
366 PALABOS in order to determine the RVE for permeability calculation. The entire process  
367 was repeated for all the binder content-grain size combinations listed in Table 1.

368



369

370 **Fig. 4.** Images of different dimensions used to determine the Representative Volume Element  
371 (RVE) of the BGLB specimen. Pores are displayed in white and silica sand grains in black on  
372 the binary image.

373

374 The numerical simulations were performed by using the open-source Lattice-Boltzmann  
375 Method (LBM) solver PALABOS (Parallel Lattice Boltzmann Solver). LBM is highly  
376 reliable and has been applied extensively as discussed by (Chopard B et al., 2002). (Heijs and  
377 Lowe, 1995) used LBM to predict the permeability of a random array of spheres and clay soil,  
378 and found that the predicted permeability is consistent with the experimentally measured  
379 values. (Ferrol and Rothman, 1995) studied the numerical simulations of mass transport  
380 through 3D tomographic images of Fontainebleau sandstone, and found that the LBM  
381 simulations were similar as compared to the finite difference calculations and with the  
382 laboratory experimental measurements. It was studied and verified earlier by (Auzerais et al.,  
383 1996) that X-ray micro computed tomography ( $\mu$ -CT) along with LBM can be used for  
384 modeling the fluid flow phenomena through complex porous geometries to study the  
385 permeability. (Degruyter et al., 2010) combined X-ray  $\mu$ -CT and LBM solver PALABOS to  
386 perform numerical simulations of gas flow through volcanic pumices, and validated the  
387 method by comparing the resulting data with the experimentally obtained values. Hence for  
388 the present numerical simulation, LBM was used to predict the permeability of the additively  
389 processed sand mold.

390

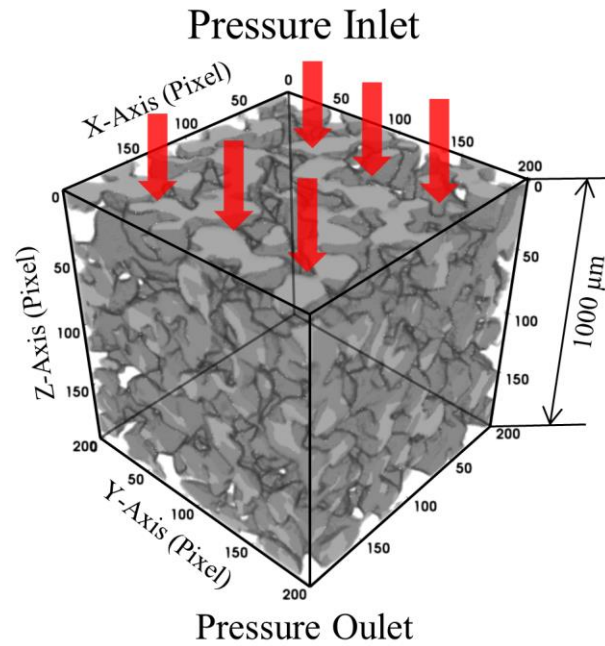
391 For the numerical simulation of mass transport through the 3D tomographic image of 3DP  
392 specimen, a bounce-back boundary condition (no-slip boundary condition) was applied in  
393 between the interfaces of pore space and silica sand grains. In PALABOS-LBM numerical

394 simulation, a D3Q19 lattice scheme is proposed as demonstrated earlier by (Hecht and  
395 Harting, 2008). D3Q19 lattice describes the fluid flow in three dimensions with 19 possible  
396 velocity vector directions, along with the zero velocity as shown by (Hecht and Harting,  
397 2008) and (Ding and Xu, 2018). A standard Bhatnagar Gross-Krook (BGK) collision operator  
398 was applied to the D3Q19 lattice scheme. A constant pressure gradient ( $\nabla P$ ) was applied  
399 through the porous medium, and the initial velocity within the interstices was set to zero. The  
400 imposed values of  $\nabla P$  were low enough to ensure creeping flow regime (Darcy flow). Non-  
401 slip boundary conditions were applied and the lateral boundaries of the porous geometry  
402 shown in Fig. 5. Permeability ( $k$ ) was then measured on the non-dimensional lattice unit  
403 system from the obtained pressure and velocity maps using Darcy's equation:

$$-\frac{dP}{dz} = \frac{\mu}{k} v \quad (7)$$

404  
405  
406 where  $dP/dz$  is the pressure gradient along the main flow  $z$ -direction,  $\mu$  is the dynamic  
407 viscosity,  $v$  is Darcy velocity and  $k$  is the permeability of the 3DP mold. The calculation  
408 methodology used by PALABOS to measure the permeability of porous media involves in  
409 solving a modified version of the actual Darcy's equation. Here,  $Q/A$  is denoted by the term  $v$ ,  
410 which is the mean fluid velocity through the porous media or as stated earlier as Darcy's  
411 velocity.  $Q$  is the flow rate of fluid through a sample of cross section area  $A$ .

412



413

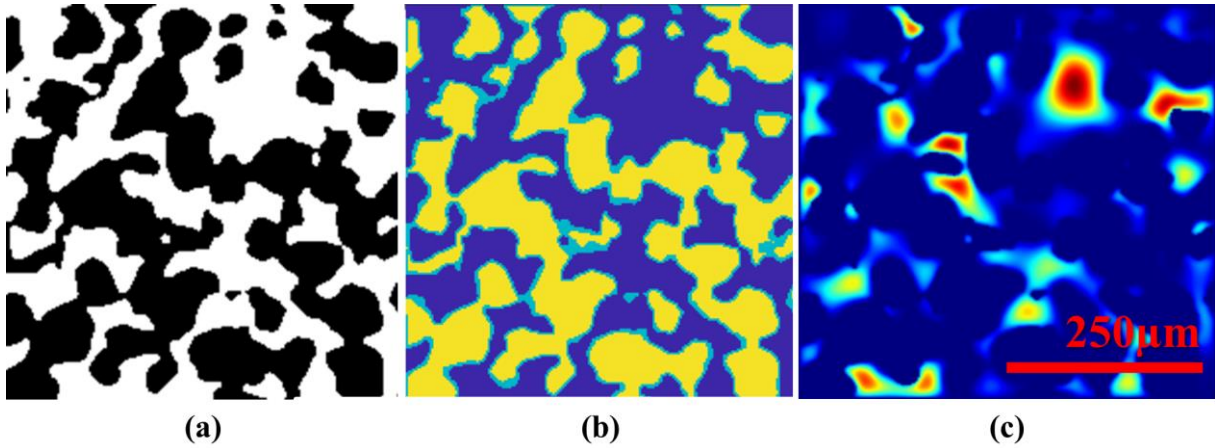
414

**Fig. 5.** Boundary conditions for numerical simulation

415

416 For the numerical simulation, the binary image was converted into a .DAT-file as needed by  
 417 PALABOS software to be able to read the entire porous 3D printed sand mold geometry  
 418 (along with labeled pores and grains), Fig 6. The DAT-file conversion procedure along with  
 419 the code for MATLAB was used from the tutorial as provided in the PALABOS website by  
 420 (Degruyter et al., 2010). The code allows for the separation between grains and pores, by  
 421 creating an interfacial boundary, as shown in Fig. 6(b). Then a constant pressure was imposed  
 422 at the inlet of the geometry. The bounce-back boundary condition was applied to the interface.  
 423 Fig. 6(c). shows an example of simulated velocity distribution over a 2D cross-section of an  
 424 X-ray  $\mu$ -CT image.  $k$  was first obtained in non-dimensional lattice units and was then  
 425 converted to SI units by considering the squared resolution of the original  $\mu$ -CT image.

426



427

428 **Fig. 6.** Visualization of steps in conversion of a  $\mu$ -CT image for velocity distribution  
 429 simulation in the case of the SGHB specimen (200 voxels): (a) 2D slice of the binary volume  
 430 and (b) converted image for simulation with pore space (dark blue pixel), grains (yellow  
 431 pixel) and grain boundary interface (light blue pixel) where the bounce-back boundary  
 432 condition is implemented. (c) Simulated velocity distribution through a cross-section.

433

#### 434 **2.4. Pore network extraction from micro-CT images: pore and throat size distributions**

435

436 A PNM approach was followed in order to characterize the dimensions of the pore bodies and  
 437 constrictions of the 3DP molds, by using the images displayed in Fig. 7 as inputs. In the  
 438 present work, the pores and the throat networks were then extracted from the obtained X-ray  
 439  $\mu$ -CT of the 3DP specimens using the SNOW and GETNET algorithm as shown by (Gostick,  
 440 2017). This algorithm was previously implemented on various porous medium ranging from  
 441 fibrous mats to sandstone, for the extraction of pore and throat sizes, and predicting  
 442 permeability values. The open-source algorithm called as SubNetwork of the Oversegmented  
 443 Watershed (SNOW) as provided by (Gostick, 2017) was utilized in the current investigation  
 444 the extract the pore-network from the X-ray  $\mu$ -CT images. The extracted pore and throat

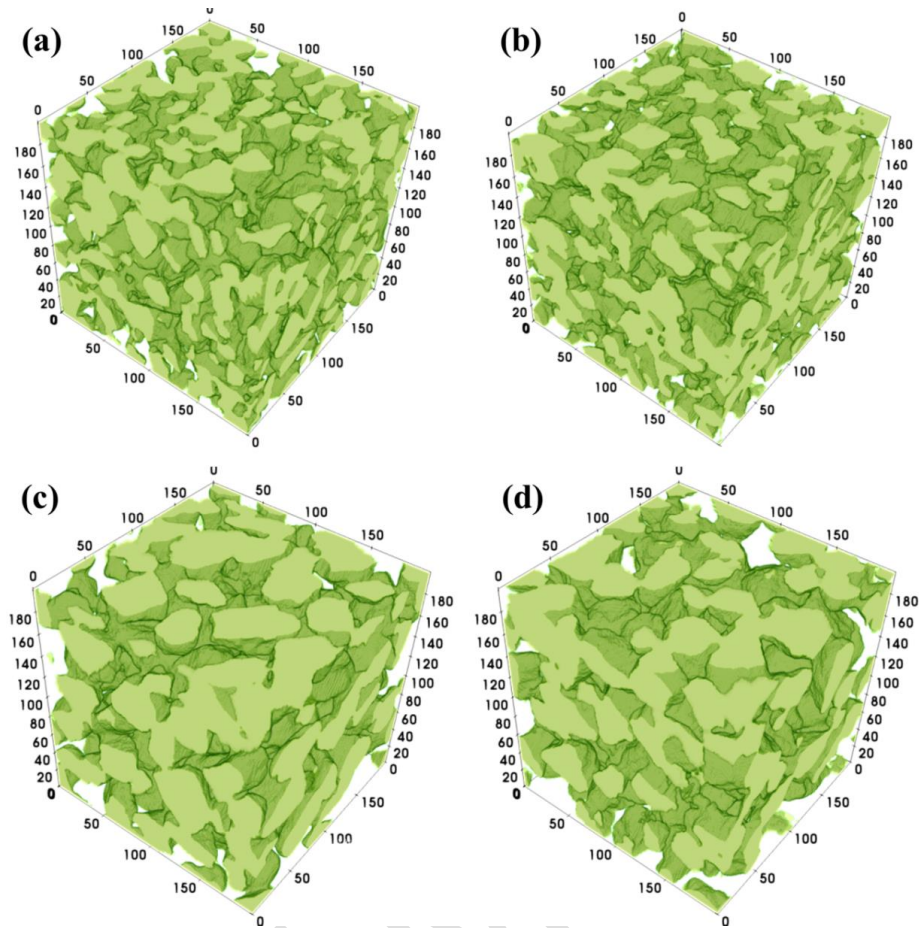
445 diameters correspond to the diameter of the largest spheres that can be inscribed in a pore  
446 body and a constriction, respectively.

447

448 The method for pore network extraction starts by using GETNET.py code as provided by  
449 (Gostick, 2017), which extracts a conventional pore network from the provided  $\mu$ -CT image  
450 of voxel size  $200^3$ . As stated by (Gostick, 2017) the code works in 4 steps, first it extracts the  
451 distance map of the pore space (distance transform), secondly a filter was used on the distance  
452 map to smoothen the image and to remove the saddles and the plateaus, thirdly merging the  
453 peaks that are too close to each other and then lastly assigning the pore space voxel to the  
454 appropriate pores using a marker-based watershed algorithm. Recently, (Rodríguez de Castro  
455 and Agnaou, 2019) have used the code to extract the pore and throat network of a sandy  
456 porous structure. Similarly, for the present extraction, the X-ray  $\mu$ -CT image of 3DP specimen  
457 was first thresholded and then converted into an 8-bit file. Then, using the SNOW algorithm  
458 in PYTHON, the X-ray  $\mu$ -CT image is imported for further characterization. This import class  
459 then extracts all the information of the provided  $\mu$ -CT image, such as pore and throat sizes,  
460 their locations and their network connectivity. All pore and throat properties are stored in  
461 Numpy arrays, which can be easily accessible at later stage for generating the network.

462





463

464 **Fig 7.** X-ray  $\mu$ -CT image for all specimens used for PNM, (a) SGLB, (b) SGHB, (c) BGLB  
 465 and (d) BGHB

466 Permeability is strongly related to the dimension of the pore constrictions (throats), as most  
 467 pressure loss is generated in these regions. (Bonnet et al., 2008) studied in detail the effect of  
 468 form, shape, or structure on flow law properties in metallic foams. On the other hand,  
 469 (Degruyter et al., 2009) and (Degruyter et al., 2010) showed that the tortuosity ( $\tau$ ), porosity ( $\varepsilon$ )  
 470 can be directly correlated according to Archie's law ( $\tau^2 = \varepsilon^{-m}$ ). (Huang et al., 2015) also  
 471 studied the flow properties within a digital image of fibrous porous medium to predict the  
 472 permeability and validated the described model. (Degruyter et al., 2009) and (Degruyter et al.,  
 473 2010) also developed a model to calculate  $k$  directly from the characteristic diameter of the  
 474 throats ( $d_{throat}$ ) and Archie's law:

475

$$k = \frac{\varepsilon^m d_{\text{throat}}^2}{32} \quad (8)$$

476

477 The permeability was then calculated by using the average throat size provided by the  
478 network model.

479

### 480 ***2.5. Experimental approach: Local porosity and permeability***

481

482 A detailed review of experimental characterization for density, porosity and permeability  
483 method was published recently by (Mitra et al., 2018) and (Mitra et al., 2019), so this section  
484 contains only a short description of the method. The weight of the 3D printed specimens was  
485 measured using a laboratory precision balance and the density of printed sample was  
486 measured as mass divided by volume. The experimentally measured density of 3D printed  
487 sand mold was  $\sim 1.3 \text{ g/cm}^3$ . The particle density is the density of silica sand with  $\sim 2.6 \text{ g/cm}^3$ .  
488 From the measured density of 3DP specimen and silica sand density, the porosity of the 3D  
489 printed samples was measured as,

490

$$\text{Porosity (\%)} = 1 - \frac{\text{Density}_{\text{bulk}}}{\text{Density}_{\text{silica}}} \quad (9)$$

491

492 The porosity values measured from experiments were close to 49-51% for all printed  
493 specimens, with a standard deviation of 0.25%. Also, the permeability of the 3DP sand mold  
494 samples was determined with a permeameter device (Simpson-Electrical), following the  
495 recommendations of the American Foundry Society (AFS) and the same procedure presented

496 in previous works by (Coniglio et al., 2017), (Sivarupan et al., 2017), (Mitra et al., 2018) and  
497 (Mitra et al., 2019). Therefore the entire procedure for the permeability experiment will not be  
498 presented here. The initial dimensions of the 3D printed parts (cylinders) for experimental gas  
499 permeability characterization were of  $49.8 \pm 0.01$  mm in length and of  $49.9 \pm 0.02$  mm in  
500 diameter. The relationship for the measurement for gas permeability (GP) is expressed by the  
501 following equation:

$$GP = \frac{V \times h}{F \times p \times t} \quad (10)$$

502

503  
504 Where  $V$  denotes the air volume,  $h$  denotes the length of the cylindrical 3DP specimen,  $F$   
505 denotes the cross-sectional area of the 3DP specimen,  $p$  denotes the pressure and  $t$  denotes the  
506 passage time for volume of air in minutes. An average permeability value of  $5.57 \times 10^{-11} \text{ m}^2$   
507 or  $\sim 56.43$  Darcy was measured for the small grain (SG) specimens, and  $9.02 \times 10^{-11} \text{ m}^2$  or  
508  $\sim 91.39$  Darcy for the big grain (BG) specimens.

509

### 510 **3. Results and discussion**

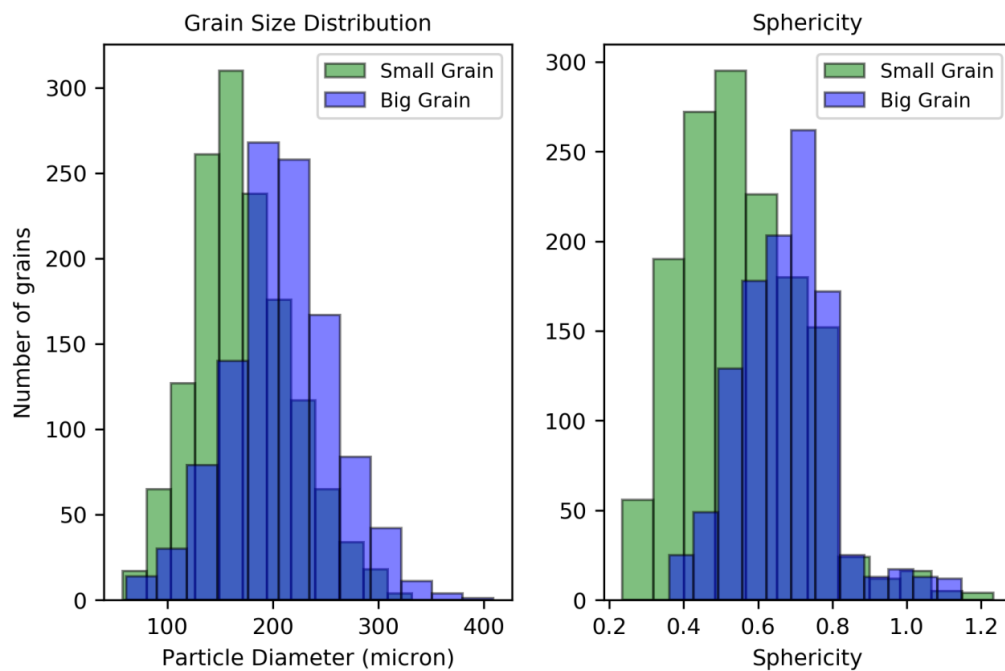
511

#### 512 ***3.1. Grain size distribution and sphericity of silica particles***

513

514 It is to be noted that since the binder was associated to the solid phase in the CT images, an  
515 individual effect of the binder cannot be assessed and therefore the values for low binder and  
516 high binder were merged together for the assessment, Fig. 8. The procedure presented in

517 subsection 2.2.2 was applied to all the segmented X-ray  $\mu$ -CT images in order to obtain the  
 518 grain size and sphericity distributions of the silica particles. A normal distribution could be  
 519 observed for the grain size distribution. The extracted silica grain diameter  $d_g$  for small grain  
 520 specimen varied from  $\sim 57 \mu\text{m}$  to  $\sim 331 \mu\text{m}$ , with mean  $d_g$  of  $\sim 171.98 \mu\text{m}$  and the extracted  $d_g$   
 521 for big grain specimen varied from  $\sim 61 \mu\text{m}$  to  $\sim 409 \mu\text{m}$ , with a mean grain diameter  $d_g$  of  
 522  $\sim 208.05 \mu\text{m}$ . A more detailed report regarding the granulometry of the 3DP specimens is  
 523 provided in Table 3, showing the values for high and lower binder contents. GSD has a  
 524 profound effect on the permeability of the 3DP sand mold. It can be seen that for both small  
 525 and bigger grains, there is a similar narrow distribution of grain sizes, hence provides good  
 526 permeability for fabricated 3DP sand mold. Because sand grains with wide range has higher  
 527 compaction leading to high density and low permeability compared to the narrow distribution.



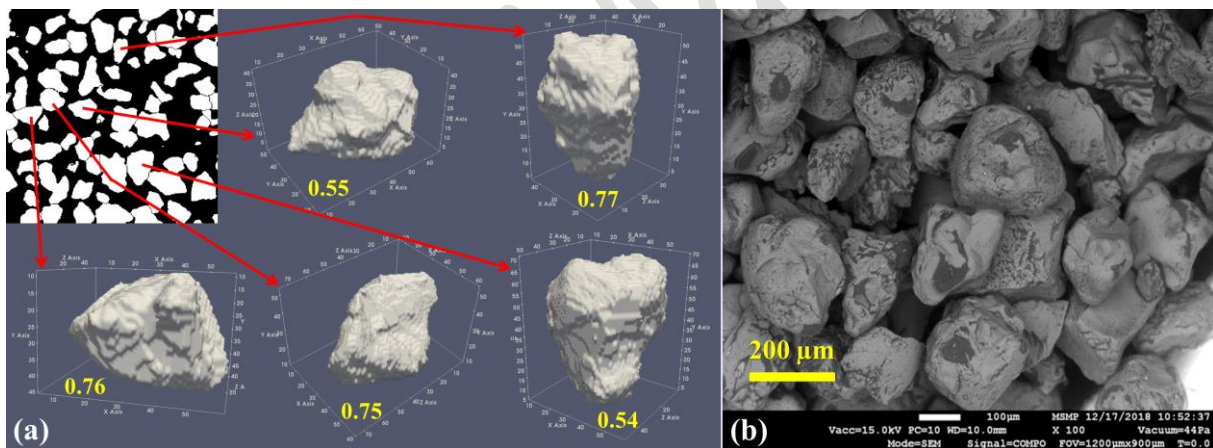
528

529 **Fig. 8.** Combined (a) grain size distribution for small grains and big grains, and (b) sphericity  
 530 distribution.

531

532 Also, the sphericity measured from the X-ray  $\mu$ -CT image provides information about the  
533 particle shape, which affects grain packing density, hence varying porosity and permeability.  
534 We note the fact that grains with different shape might have identical sphericity values. The  
535 results in terms of sphericity are listed in Table 3. It is observed that the sphericity values of  
536 the bigger grain size specimens were higher than those of the small grain size specimens.  
537 Some examples of extracted grains from the big grain specimens are shown in Fig. 9. It can be  
538 noticed that the grains are far from being a perfect sphere, with an average sphericity value of  
539  $\sim 0.6$ . As we discussed earlier the shape can be rounded, angular, sub-angular, however in the  
540 present case, it can be observed that the grains are mostly sub-angular. All the results of the  
541 sphericity of the specimens are shown as a histogram in Fig. 8.

542



543

544 **Fig. 9.** (a) Examples of silica grain with different sphericity number in the BG specimen. (b)  
545 SEM image of a 3DP specimen, showing the silica grains.

546

547 From the obtained granulometry, using the porosity and mean grain diameter, the  
548 permeability of the 3DP specimens were predicted with the Kozeny-Carman equation (Eq. 3)  
549 as shown in Table 3. It is to be noted that since the binder was associated to the solid phase in

550 the CT images, an individual effect of the binder cannot be assessed and therefore the values  
551 for low binder and high binder are very close.

552

553 **Table 3.** Results from image analysis

Sample Type	Mean $d_g$ ( $\mu\text{m}$ )	Mean Sphericity	Mean porosity (%)	Permeability ( $\text{m}^2$ )	Permeability (Darcy)
<i>SGLB</i>	154.07	0.56	50.97	$6.593 \times 10^{-11}$	66.80
<i>SGHB</i>	156.85	0.55	49.37	$6.182 \times 10^{-11}$	62.63
<i>BGLB</i>	210.11	0.66	48.48	$1.003 \times 10^{-10}$	101.62
<i>BGHB</i>	207.04	0.67	49.35	$1.077 \times 10^{-10}$	109.12

554

555 **3.2. Permeability of the printed samples as obtained from LBM numerical simulations**

556

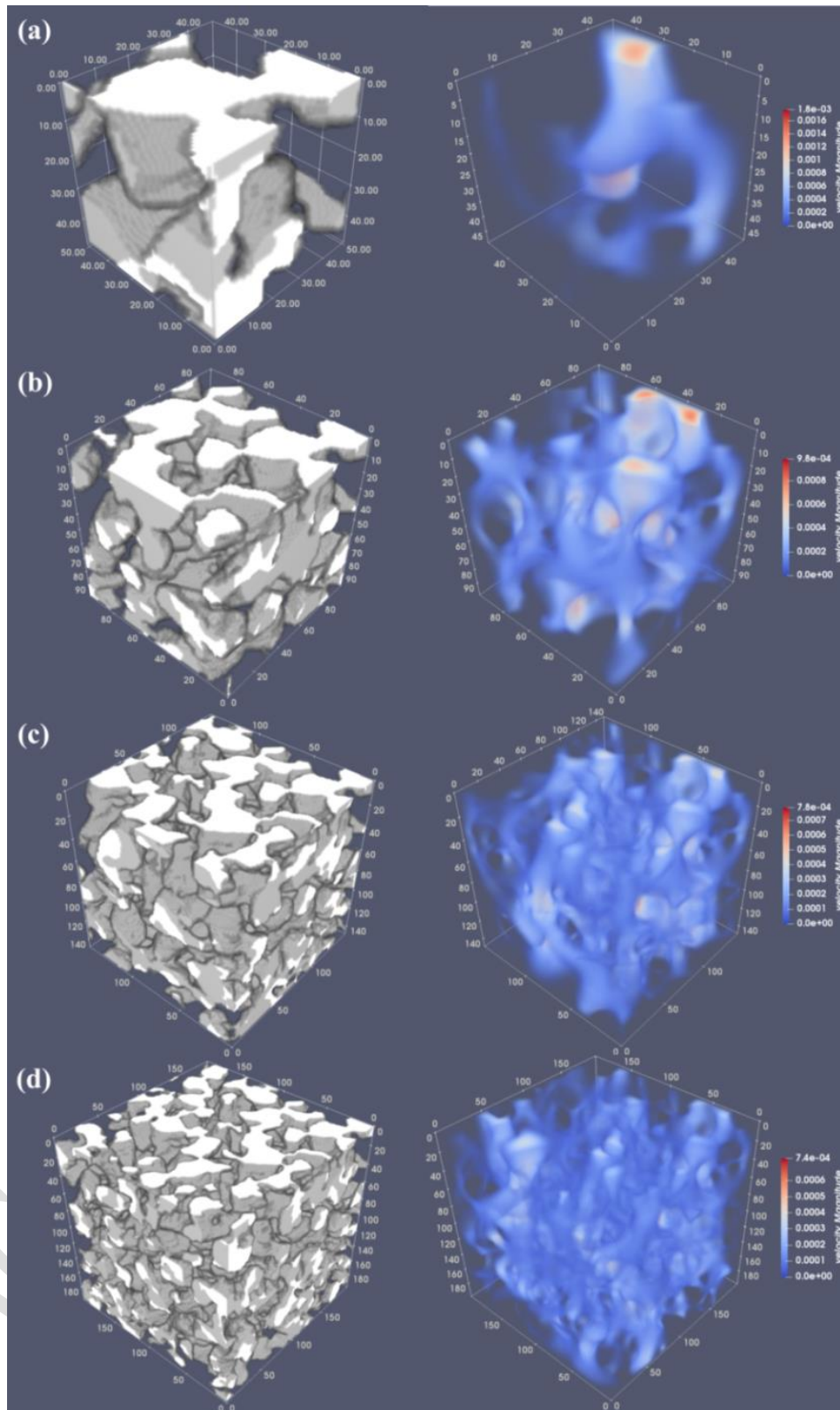
557 The steady-state velocity maps provided by the LBM simulations introduced in subsection  
558 2.3., throughout the simulated specimens were represented using PARAVIEW software as  
559 shown in Fig. 10. It can be deduced from this figure that the velocity distribution is not  
560 uniform throughout the porous media, as expected due to the varying cross-section  
561 dimensions of the interstices. The ratio between pressure difference ( $\Delta P$ ) and the volumetric  
562 flow rate was constant for all the tested values of  $\Delta P$ , confirming creeping regime. Different  
563 image sizes ( $50^3$  voxel,  $100^3$  voxel,  $150^3$  voxel, and  $200^3$  voxel) were used in the simulations  
564 for the computation of  $k$ . Table 4 provides the permeability values for all the specimens as  
565 provided by LBM solver PALABOS by using the modified Darcy's equation (Eq. 7) as stated  
566 earlier in section 2.3. Indeed, from Fig. 11, it can be observed that the permeability value for

567 50 voxel image is lower than that of 100 voxel, 150 voxel and 200 voxel image stack for all  
568 the 3DP specimens. The permeability values approached a plateau value when the size of the  
569 RVE was greater than 100 voxels. Therefore, it is suggested to use an input volume of 500  
570  $\mu\text{m}^3$ , which corresponds to the size of 3 equivalent layers ( $3 \times 190 \mu\text{m}$  or  $3 \times 140 \mu\text{m}$ ) of silica  
571 grains for 3DP specimens with average grain diameter of 140  $\mu\text{m}$  and 190  $\mu\text{m}$ . Bigger image  
572 sizes would lead to higher simulation times without any significant improvement in accuracy.

573

Accepted Manuscript





574

575 **Fig. 10.** Velocity map in lattice units through specimens of, (a) 50, (b) 100, (c) 150, and (d)

576

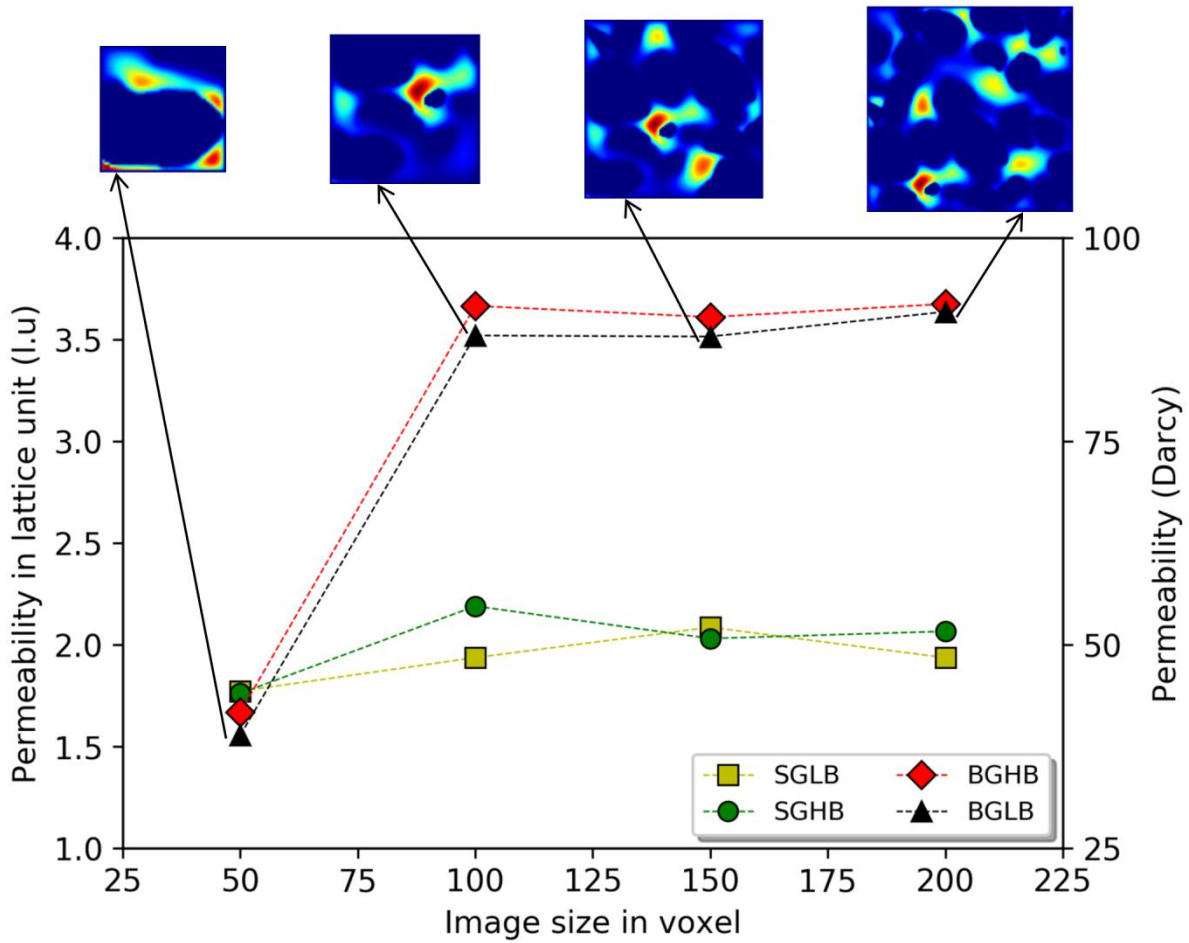
200 voxel. (Warmer colors represent higher velocity)

577



**Table 4.** Results from permeability simulation

<b>Image Size (voxel)</b>	<b>Porosity (%)</b>	<b>Permeability (m<sup>2</sup>)</b>	<b>Permeability (Darcy)</b>
<i>Small Grain Low Binder (SGLB)</i>			
50	51	$4.431 \times 10^{-11}$	44.89
100	50	$4.844 \times 10^{-11}$	49.08
150	51	$5.215 \times 10^{-11}$	52.84
200	52	$4.842 \times 10^{-11}$	49.06
<i>Small Grain High Binder (SGHB)</i>			
50	49	$4.403 \times 10^{-11}$	44.61
100	51	$5.475 \times 10^{-11}$	55.47
150	50	$5.077 \times 10^{-11}$	51.44
200	53	$5.166 \times 10^{-11}$	52.34
<i>Big Grain Low Binder (BGLB)</i>			
50	49	$3.889 \times 10^{-11}$	39.41
100	51	$8.801 \times 10^{-11}$	89.17
150	49	$8.788 \times 10^{-11}$	89.04
200	52	$9.092 \times 10^{-11}$	92.12
<i>Big Grain High Binder (BGHB)</i>			
50	49	$4.171 \times 10^{-11}$	42.26
100	52	$9.157 \times 10^{-11}$	92.78
150	53	$9.027 \times 10^{-11}$	91.46
200	53	$9.189 \times 10^{-11}$	93.11



581

582 **Fig. 11.** Effect of input geometry volume on the computed value of permeability

583

584 The computed results of permeability for 3DP specimen through PALABOS with different  
 585 grain and binder percent samples can be compared with the predicted analytical results and  
 586 image analysis results. The agreement is good between the analytical method, the image  
 587 analysis and the experimental results for all the 3DP specimens (SGLB, SGHB, BGLB, and  
 588 BGHB). The permeability calculations obtained with PALABOS are in good co-relation with  
 589 the experimental measurements performed with the 3DP specimen, as shown in Table 4.  
 590 Although it is of worth mentioning that an analytical permeability value of  $4.9 \times 10^{-11} \text{ m}^2$  (or)  
 591  $\sim 49$  Darcy was calculated with Kozeny-Carmen equation (Eq 3), by using the average grain  
 592 size of 140 micron (as provided by the ExOne sand provider) and measured porosity of 49.2

593 %. And also a permeability of  $9.071 \times 10^{-11} \text{ m}^2$  (or) ~91 Darcy was calculated) with the  
594 average grain size of 190 micron (as provided by the ExOne sand provider) and measured  
595 porosity of 49.5 %. A deviation of permeability could be observed compared to analytical  
596 permeability value as the prediction of Kozeny-Carmen is based on the particles being a  
597 perfect sphere (the equation uses the mean diameter,  $d_s$ ), whereas in the present scenario the  
598 particle is close to being a perfect sphere (average sphericity = 0.65). The analytically  
599 predicted permeability value using Kozeny-Carmen equation worked as a reference for the  
600 permeability measurements. It can be observed from the table that, it is possible to predict the  
601 absolute permeability of 3DP sand mold using the non-destructive LBM simulation and is a  
602 very strong method for mass flow simulation in complex 3D printed sand mold.

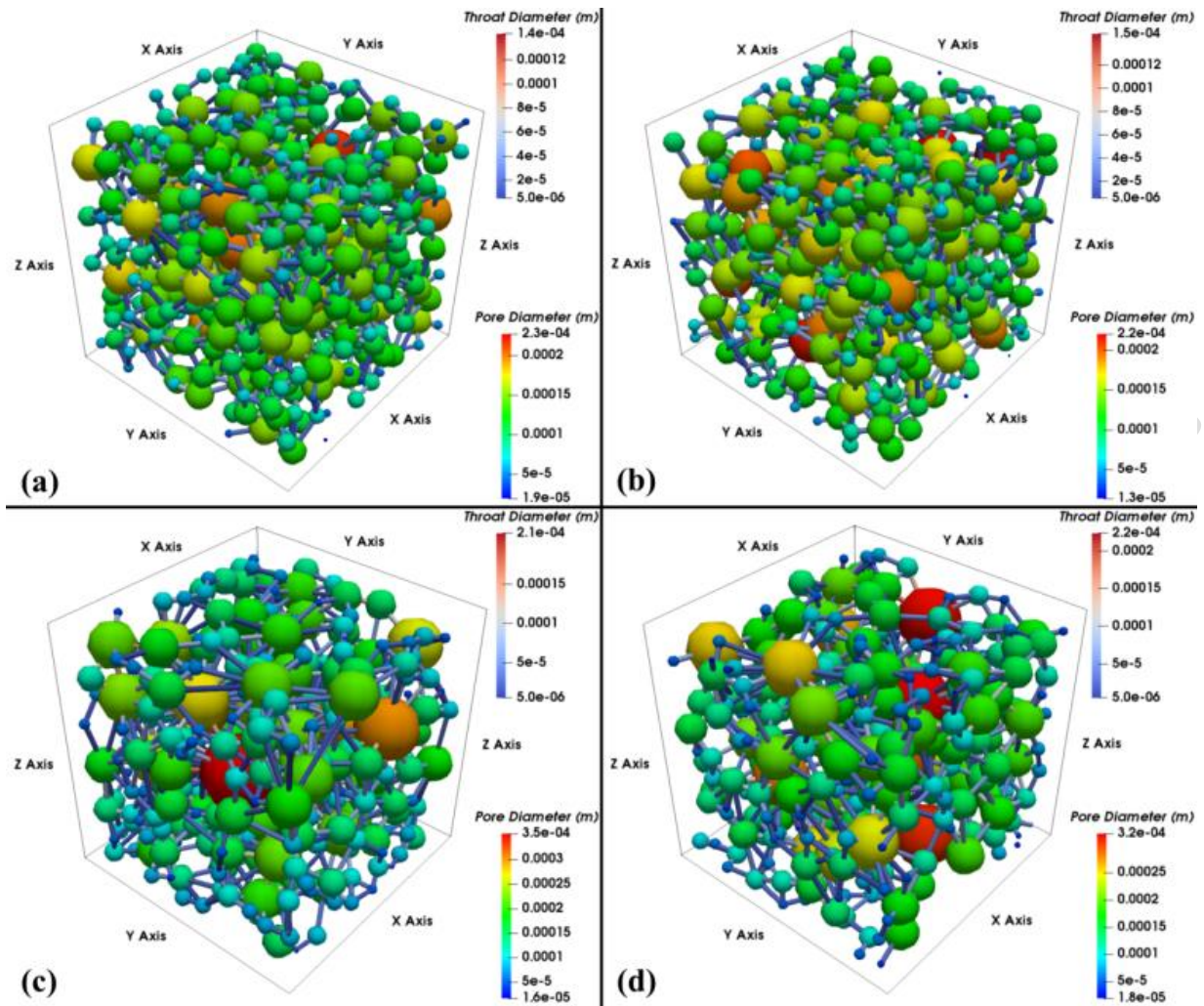
603

### 604 ***3.3. Pores and Throats Size Distributions of the 3D printed samples as provided by pore-*** 605 ***network modeling***

606

607 PNM provides a reasonable prediction of mass transport properties at pore scale and offers the  
608 flexibility of characterizing macroscopic properties relationship of 3DP sand mold with pore  
609 structure. With PNM, the complex pore structure of a 3DP sand mold can be represented by a  
610 network of pores (pore spaces) and connected throats (narrow paths that connect pores) with  
611 simplified geometries. A pore network modeling aims at better representation of pore and  
612 throat interconnectivity in a porous medium like 3DP sand mold. All the pore network  
613 extractions for different specimens (SGLB, SGHB, BGLB, BGHB) were performed over a  $\mu$ -  
614 CT image size of  $200^3$  voxel with a resolution of  $5 \mu\text{m}$  per voxel, and are represented in Fig.  
615 12.

616



617

618

**Fig. 12.** Extracted pore network for (a) SGLB, (b) SGHB, (c) BGLB and (d) BGHB

619

specimens.

620

621

The pore-size distributions (PSDs) in terms of pore diameter were extracted from the

622

generated pore network and are represented as a histogram, Fig. 13. The extracted pore

623

diameter for SGLB specimen varied from  $\sim 19 \mu\text{m}$  to  $\sim 226 \mu\text{m}$ , with a mean pore diameter of

624

$\sim 105.84 \mu\text{m}$  and the extracted pore diameter for SGHB specimen varied from  $\sim 14 \mu\text{m}$  to  $\sim 220$

625

$\mu\text{m}$ , with a mean pore diameter of  $108.05 \mu\text{m}$ . Similarly, the extracted pore diameter for

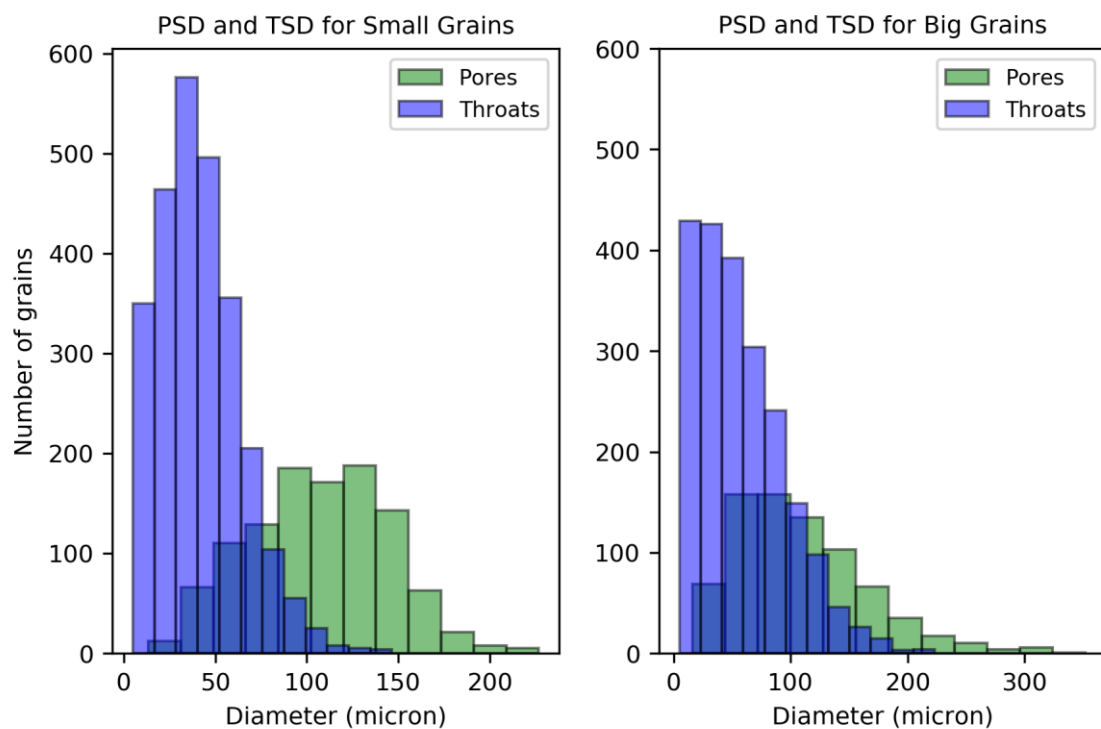
626

BGLB specimen varied from  $\sim 16 \mu\text{m}$  to  $\sim 350 \mu\text{m}$ , with a mean pore diameter of  $108.07 \mu\text{m}$

627

and the extracted pore diameter for BGHB specimen varied from  $\sim 18 \mu\text{m}$  to  $\sim 320 \mu\text{m}$ , with a

628 mean pore diameter of  $\sim 108.31 \mu\text{m}$ . Although previous work by (Glover and Walker, 2009)  
 629 showed that the grain size and pore radius are functionally interdependent, it can be observed  
 630 that the average pore diameters are very similar for all the specimens (both SG and BG) in the  
 631 currently investigated samples. However, careful observation of Fig. 13 shows that the  
 632 standard deviation of the PSD is considerably higher for the big sand grains samples ( $\pm 55.9$   
 633  $\mu\text{m}$  for BGLB and  $\pm 56.1 \mu\text{m}$  for BGHB) as compared to the small sand grains samples ( $\pm$   
 634  $37.3 \mu\text{m}$  for SGLB and  $\pm 38.7 \mu\text{m}$  for SGHB). Consequently, the size of the biggest pores in  
 635 the big grain samples is much higher than for the small grain samples, even if the average  
 636 pore size is close in both cases. This can be also observed in the red-colored pores of Fig. 12  
 637 (approximately 350 micrometers of big grains and 230 for small grains) and in the PSDs  
 638 provided in Figure 13.



640

641 **Fig. 13.** Combined (high binder +low binder) pore size and throat size distribution for (a)

642

small grains and (b) big grains.

643

644 The throat-size distributions (TSDs) in diameter were also extracted from the generated throat  
645 network and were then represented as a cumulative histogram with the throat diameter, Fig.  
646 13. The extracted throat diameter for SGLB specimen varied from  $\sim 5 \mu\text{m}$  to  $\sim 140 \mu\text{m}$ , with a  
647 mean throat diameter of  $38.66 \mu\text{m}$  and the extracted throat diameter for SGHB specimen  
648 varied from  $\sim 5 \mu\text{m}$  to  $\sim 146 \mu\text{m}$ , with a mean throat diameter of  $44.43 \mu\text{m}$ . Similarly, the  
649 extracted throat diameter for BGLB specimen varied from  $\sim 5 \mu\text{m}$  to  $\sim 214 \mu\text{m}$ , with a mean  
650 throat diameter of  $56.92 \mu\text{m}$  and the extracted throat diameter for BGHB specimen varied  
651 from  $\sim 5 \mu\text{m}$  to  $\sim 220 \mu\text{m}$ , with a mean throat diameter of  $58.42 \mu\text{m}$ . It can be depicted from  
652 the distribution that, the peak values for both cases appear to be near low pore sizes, which  
653 defines the microstructure complexity. It can also be observed for big grain specimens that the  
654 throats and pores overlap with each other, which suggests that there exist some small pores,  
655 which are of similar size as that of the throats. Moreover, the distribution of throat size for all  
656 the specimens shows a right-skewed distribution, along with a quantitatively great portion of  
657 the small size throats (peak throat size smaller than average), which construct minor flow  
658 paths.

659

660

**Table 5.** Results from pore network modeling

<b>Sample Type</b>	<b>Mean Pore Diameter (<math>\mu\text{m}</math>)</b>	<b>Mean Throat Diameter (<math>\mu\text{m}</math>)</b>	<b>Permeability (<math>\text{m}^2</math>)</b>	<b>Permeability (Darcy)</b>
<i>SGLB</i>	105.84	38.66	$3.138 \times 10^{-11}$	31.79
<i>SGHB</i>	108.05	44.43	$4.144 \times 10^{-11}$	41.98
<i>BGLB</i>	108.07	56.92	$6.915 \times 10^{-11}$	70.06
<i>BGHB</i>	108.31	58.42	$7.165 \times 10^{-11}$	72.59

661

662 From the obtained average equivalent throat diameter and tortuosity, permeability was  
663 calculated using the equation described in the previous section, Eq. 8, and the results are  
664 presented in Table 5. It can be observed from the results that no significant differences in  
665 terms of permeability ( $k$ ) were obtained for small grain samples with different binder content  
666 along with big grain samples with different binder content, as the furan resin binder was only  
667 associated to the solid phase in the  $\mu$ -CT images. An individual effect of the binder over pore  
668 network structure cannot be assessed and therefore the values for pore and throat diameter for  
669 samples with low binder and high binder are very close.

670

#### 671 **4. Model efficiency**

672

673 One of the challenges in foundry is the lack of methods for proper non-destructive  
674 characterization of the local permeability of the 3DP sand mold. The X-ray  $\mu$ CT technique  
675 overcomes this challenge and allows a non-destructive visualization and characterization of  
676 internal volume and the external surface of a sand mold. This paper, for the first time, fully  
677 characterizes the intrinsic physical parameters of 3DP sand mold including grain structure,  
678 porosity, pore connectivity, tortuosity, pore size distribution, throat size distribution and local  
679 density. Table. 6 shows the cumulative results of permeability as obtained by different  
680 methods (from traditional experiment, from GSD, from LBM and from PNM). The  
681 permeability value using the GSD method overpredicts the permeability value as obtained  
682 with the traditional experiments. Indeed, the permeability value from GSD using Kozeny-  
683 Carman equation is based on the particles being a perfect sphere (the equation uses the mean  
684 particle diameter,  $d_s$ ), whereas in the present scenario the particle is close to being a perfect

685 sphere (average sphericity = 0.65). However, the permeability value obtained with GSD using  
686 Kozeny-Carman equation can still be considered as a reference for other models.

687

688 Moreover, the permeability values yielded by LBM simulations were found to be close to the  
689 results provided by traditional tests. Nevertheless, LBM requires much computational power  
690 for larger  $\mu$ -CT images, hence this method can be time consuming. Therefore, it was crucial  
691 to identify the optimum RVE not only to predict reliable permeability values but also to  
692 reduce simulation times. An alternative approach to predict permeability from pore-network  
693 modelling (PNM) is proposed. Pores are the relatively wide portions of the interstices and  
694 throats are the relatively narrow portions that separate the pore bodies. The pores and throats  
695 space of a 3D printed sand mold can be extracted from the segmented 3D  $\mu$ -CT image. As can  
696 be observed from Table 6, significant differences are reported in some cases between the  
697 results of traditional experiments and PNM, while the agreement is better between traditional  
698 tests and GSD and LBM. Nevertheless, as compared to LBM simulations, PNM require less  
699 computational power due to the simplifications of the void-space geometry and topology  
700 when constructing the pore network model. The computational time needed for the extraction  
701 of the pore and throat network on a computer with Intel Xeon processor and 16 GB of  
702 memory is in the order of minutes, whereas using LBM computation takes hours. This allows  
703 the computation of permeability over larger sampling volumes. However, it should be noted  
704 that the computational time can be significantly reduced by using a more powerful and  
705 expensive supercomputer. (Chauveteau et al., 1996) showed that for unconsolidated porous  
706 media where pore throats are much smaller than pore bodies, the viscous dissipation can be  
707 considered as being localized only in pore throats. This approximation is quite acceptable in  
708 many cases, since the pore body-to-pore throat radius is generally quite large, varying from  
709 values around 3 for random monosized sphere packs, to around 5 for random packs of sharp-



710 edged grains with a narrow size distribution. However, in the case of the highly-porous 3DP  
 711 sand molds investigated in the present work, the pore-to-throat size ratios range from ~1.7 to  
 712 ~2.7 (Table 5). Therefore, the PNM-based estimation obtained with Eq. 8, in which viscous  
 713 dissipation is assumed to be localized only in pore throats, is not expected to be highly  
 714 accurate, but is still useful to provide a lower permeability bound. Hence, PNM approach can  
 715 be a reasonable alternative to the traditional experimental, LBM and GSD methods as it takes  
 716 into account of the microstructural features of the 3DP sand mold and can also easily deal  
 717 with any kind of complex geometry.

718

719 **Table 6.** Permeability measured with different methods

<b>Sample</b>	<b>Traditional experiment (Darcy)</b>	<b>GSD (Darcy)</b>	<b>LBM using 100 voxel (Darcy)</b>	<b>PNM (Darcy)</b>
SGLB	56.4	66.8	49	31.79
SGHB	58.9	62.6	55.4	41.98
BGLB	91.3	101.6	89.1	70.06
BGHB	93.2	109.1	92.7	72.59

720

721 Permeability, porosity, tortuosity grain size distribution, pore size distribution, average pore  
 722 diameter, throat size distribution, and average throat diameter are essential inputs when  
 723 predicting gas flow in 3DP molds. It is to be noted that complex porous media like 3DP sand  
 724 mold have anisotropic properties (mechanical and mass transport) due to variation in printing  
 725 process parameters. For the present study, only the variation of furan resin binder droplet  
 726 resolution on silica sand powder bed is studied (different binder percentage) along with  
 727 different silica grain size, as this affects the properties of complex porous resin bonded 3DP

728 mold with the recoater speed. The present modeling approaches are advantageous on the  
729 prediction of the flow permeability of such complex porous structure like 3DP sand mold  
730 directly from the from X-Ray  $\mu$ -CT digital images. This would help the foundry industry to  
731 accurately measure the mass transport properties as required as an input for numerical  
732 simulations (solidification and filling), to study the effect of printing process parameters  
733 (printing speed, binder percentage, grain size, etc.) and thermal degradation of furan resin  
734 binder during metal casting. Therefore, the present approaches of merging permeability  
735 measurements on 3DP sand mold specimens with extraction of throat and pore network  
736 structure using for X-ray  $\mu$ -CT helped in exploring and better understanding the pore  
737 construction and its pivotal role on mass flow phenomenon. It also helped us in developing  
738 and validating reliable models for non-destructive prediction of gas permeability, which are  
739 favorable for carrying out precise risk assessments of harmful toxic pollutants produced  
740 during metal casting in foundry industry.

741

## 742 **5. Conclusion**

743

744 Permeability is one of the most important factors affecting the generation of gas defects  
745 during metal casting, so it is of major importance to characterize it. In this work, the  
746 advantage of the application of X-ray  $\mu$ -CT (NDT), Pore Network Modelling methods and  
747 Lattice Boltzmann Method in exploring the mass transport properties of additively processed  
748 silica sand mold was demonstrated. X-ray  $\mu$ -CT images were used to compute the porosity,  
749 pore size, throat size and the permeability of the 3D printed specimens for different binder  
750 contents and grain sizes, using analytical and numerical methods. The permeability predicted  
751 in the steady-state was compared with experimental and analytical measurements for layered

752 silica grain arrangement. A major advantage of using X-ray CT characterization is the non-  
753 destructive nature of the tests. The computed permeability can be used as input to numerical  
754 simulations of metal casting allowing the prediction of macroscopic defects. The following  
755 scientific and industrial implications are drawn from the present work:

756

757 • The permeability values predicted with LBM from X-ray  $\mu$ -CT image of 3DP specimen  
758 are in good agreement with the traditional experimental measurements.

759

760 • The proposed non-destructive X-ray  $\mu$ -CT technique is an effective and reliable  
761 alternative to traditional laboratory experiments for permeability characterization of  
762 additively processed sand molds. The good agreement between the analytical model,  
763 traditional experimental estimations and the proposed method based on CT data validates  
764 this approach.

765

766 • An RVE of  $100 \times 100 \times 100$  voxel corresponding to  $500 \times 500 \times 500 \mu\text{m}^3$  is suggested for a  
767 faster and reliable permeability simulation.

768

769 • The characterization of the 3D printed specimen was performed by using available open-  
770 source software such as ImageJ, Palabos, and OpenPNM and therefore the proposed  
771 approach may be used in a broad range of academic or research applications.

772

773 • The permeability value predicted using pore network modeling can be a reasonable  
774 alternative as it takes into account of the microstructural features of the 3DP sand mold.

775

776 The present findings represent a step forward towards improved prediction of mass transport  
777 properties of the 3DP sand molds. However, further characterization of permeability of such  
778 additively processed sand mold should be performed with varying average grain diameter, to  
779 check the convergence of the present model. Also samples printed with other printing process  
780 parameters should be studied.

781

782

## 783 **6. Acknowledgment**

784

785 The assistance of Mr. Jérémie Bourgeois with the 3D printing of sand specimens is greatly  
786 appreciated.

787

788

789

790

791

792

793

794

795

796 **References**

- 797 Almaghariz, E.S., 2015. Determining When to Use 3D Sand Printing : Quantifying the Role  
798 of Complexity By Eyad S . Almaghariz A thesis Submitted in Partial Fulfillment of the  
799 Requirements for the Degree of Master of Science in the.
- 800 Almaghariz, E.S., Conner, B.P., Lenner, L., Gullapalli, R., Manogharan, G.P., Lamoncha, B.,  
801 Fang, M., 2016. Quantifying the role of part design complexity in using 3d sand printing  
802 for molds and cores. *Int. J. Met.* 10, 240–252. [https://doi.org/10.1007/s40962-016-0027-](https://doi.org/10.1007/s40962-016-0027-5)  
803 5
- 804 Anbar, S., Thompson, K.E., Tyagi, M., 2019. The Impact of Compaction and Sand Migration  
805 on Permeability and Non-Darcy Coefficient from Pore-Scale Simulations. *Transp.*  
806 *Porous Media* 127, 247–267. <https://doi.org/10.1007/s11242-018-1190-3>
- 807 Auzeais, F.M., Dunsmuir, J., Ferréol, B.B., Martys, N., Olson, J., Ramakrishnan, T.S.,  
808 Rothman, D.H., Schwartz, L.M., 1996. Transport in sandstone: A study based on three  
809 dimensional microtomography. *Geophys. Res. Lett.* 23, 705–708.  
810 <https://doi.org/10.1029/96GL00776>
- 811 Ayachit Utkarsh, 2015. *The ParaView Guide: A Parallel Visualization Application*, Kitware.
- 812 Boek, E.S., Venturoli, M., 2010. Lattice-Boltzmann studies of fluid flow in porous media  
813 with realistic rock geometries. *Comput. Math. with Appl.* 59, 2305–2314.  
814 <https://doi.org/10.1016/j.camwa.2009.08.063>
- 815 Bonnet, J.P., Topin, F., Tadrist, L., 2008. Flow laws in metal foams: Compressibility and pore  
816 size effects. *Transp. Porous Media* 73, 233–254. [https://doi.org/10.1007/s11242-007-](https://doi.org/10.1007/s11242-007-9169-5)  
817 9169-5

818 Boulos, V., Fristot, V., Houzet, D., Salvo, L., Lhuissier, P., 2013. Investigating performance  
819 variations of an optimized GPU-ported granulometry algorithm To cite this version :  
820 Investigating performance variations of an optimized GPU-ported granulometry  
821 algorithm. Des. Archit. Signal Image Process. (DASIP), 2012 Conf. on, Oct 2012,  
822 Karlsruhe, Ger. 1–6.

823 Chauveteau, G., Nabzar, L., El Attar, Y., Jacquin, C., 1996. Pore Structure and  
824 Hydrodynamics, in: SCA Conference Paper Number 9607.

825 Chopard B, Dupuis A, Masselot A, Luthi P, 2002. Cellular Automata and Lattice Boltzmann  
826 techniques: an approach to model and simulate complex systems. Adv. Complex Syst.  
827 05, 101–102. <https://doi.org/10.1142/S0219525902000560>

828 Coniglio, N., Sivarupan, T., El Mansori, M., 2017. Investigation of process parameter effect  
829 on anisotropic properties of 3D printed sand molds. Int. J. Adv. Manuf. Technol.  
830 <https://doi.org/10.1007/s00170-017-0861-5>

831 De Chiffre, L., Carmignato, S., Kruth, J.P., Schmitt, R., Weckenmann, A., 2014. Industrial  
832 applications of computed tomography. CIRP Ann. - Manuf. Technol. 63, 655–677.  
833 <https://doi.org/10.1016/j.cirp.2014.05.011>

834 Degruyter, W., Bachmann, O., Burgisser, A., 2009. Controls on magma permeability in the  
835 volcanic conduit during the climactic phase of the Kos Plateau Tuff eruption (Aegean  
836 Arc). Bull. Volcanol. 72, 63–74. <https://doi.org/10.1007/s00445-009-0302-x>

837 Degruyter, W., Burgisser, A., Bachmann, O., Malaspinas, O., 2010. Synchrotron X-ray  
838 microtomography and lattice Boltzmann simulations of gas flow through volcanic  
839 pumices. Geosphere 6, 470–481. <https://doi.org/10.1130/GES00555.1>

840 Ding, W.T., Xu, W.J., 2018. Study on the multiphase fluid-solid interaction in granular

841 materials based on an LBM-DEM coupled method. *Powder Technol.* 335, 301–314.  
842 <https://doi.org/10.1016/j.powtec.2018.05.006>

843 ExOne, 2014. FB001 (Furan Binder) - Fiche De Données De Sécurité Caprolactam, selon  
844 1907/2006/CE, Article 31.

845 ExOne, 2013. FS001 ( Silica sand )-Material data sheet.

846 Ferrol, B., Rothman, D.H., 1995. Lattice-Boltzmann simulations of flow through  
847 Fontainebleau sandstone. *Transp. Porous Media* 20, 3–20.  
848 <https://doi.org/10.1007/BF00616923>

849 FLANNERY, B.P., DECKMAN, H.W., ROBERGE, W.G., D'AMICO, K.L., 1987. Three-  
850 Dimensional X-ray Microtomography. *Science* (80-. ). 237, 1439–1444.  
851 <https://doi.org/10.1126/science.237.4821.1439>

852 Glover, P.W.J., Walker, E., 2009. Grain-size to effective pore-size transformation derived  
853 from electrokinetic theory. *Geophysics* 74. <https://doi.org/10.1190/1.3033217>

854 Gostick, J., Aghighi, M., Hinebaugh, J., Tranter, T., Hoeh, M.A., Day, H., Spellacy, B.,  
855 Sharqawy, M.H., Bazylak, A., Burns, A., Lehnert, W., Putz, A., 2016. OpenPNM: A  
856 Pore Network Modeling Package. *Comput. Sci. Eng.* 18, 60–74.  
857 <https://doi.org/10.1109/MCSE.2016.49>

858 Gostick, J.T., 2017. Versatile and efficient pore network extraction method using marker-  
859 based watershed segmentation. *Phys. Rev. E* 96, 1–15.  
860 <https://doi.org/10.1103/PhysRevE.96.023307>

861 Hawaldar, N., Zhang, J., 2018. A comparative study of fabrication of sand casting mold using  
862 additive manufacturing and conventional process. *Int. J. Adv. Manuf. Technol.* 97,

863 1037–1045. <https://doi.org/10.1007/s00170-018-2020-z>

864 Hazlett, R.D., 1995. Simulation of capillary-dominated displacements in microtomographic  
865 images of reservoir rocks. *Transp. Porous Media* 20, 21–35.  
866 <https://doi.org/10.1007/BF00616924>

867 Hecht, M., Harting, J., 2008. Implementation of on-site velocity boundary conditions for  
868 D3Q19 lattice Boltzmann 1–14. <https://doi.org/10.1088/1742-5468/2010/01/P01018>

869 Heijs, A.W.J., Lowe, C.P., 1995. Numerical evaluation of the permeability and the Kozeny  
870 constant for two types of porous media. *Phys. Rev. E* 51, 4346–4352.  
871 <https://doi.org/10.1103/PhysRevE.51.4346>

872 Hormann, K., Baranau, V., Hlushkou, D., Höltzel, A., Tallarek, U., 2016. Topological  
873 analysis of non-granular, disordered porous media: Determination of pore connectivity,  
874 pore coordination, and geometric tortuosity in physically reconstructed silica monoliths.  
875 *New J. Chem.* 40, 4187–4199. <https://doi.org/10.1039/c5nj02814k>

876 Huang, X., He, Y., Zhou, W., Deng, D., Zhao, Y., 2019. Pore network modeling of fibrous  
877 porous media of uniform and gradient porosity. *Powder Technol.* 343, 350–361.  
878 <https://doi.org/10.1016/j.powtec.2018.11.022>

879 Huang, X., Wang, Q., Zhou, W., Deng, D., Zhao, Y., Wen, D., Li, J., 2015. Morphology and  
880 transport properties of fibrous porous media. *Powder Technol.* 283, 618–626.  
881 <https://doi.org/10.1016/j.powtec.2015.06.015>

882 Ignacio Arganda-Carreras, Rodrigo Fernandez-Gonzalez, Arrate Munoz-Barrutia, Carlos  
883 Ortiz-De-Solorzano, 2010. 3D reconstruction of histological sections: Application to  
884 mammary gland tissue. *Microsc. Res. Tech.* 73, 1019–1029.



885 Jaganathan, S., Vahedi Tafreshi, H., Pourdeyhimi, B., 2008. A realistic approach for modeling  
886 permeability of fibrous media: 3-D imaging coupled with CFD simulation. *Chem. Eng.*  
887 *Sci.* 63, 244–252. <https://doi.org/10.1016/j.ces.2007.09.020>

888 Kadauw, A., 2014. Characterization of the parameters of sand moulds in compaction process  
889 by use of the industrial computer tomography (ICT). *Arch. Metall. Mater.* 59, 1097–  
890 1101. <https://doi.org/10.2478/amm-2014-0189>

891 Latt J, 2009. Palabos, Parallel Lattice Boltzmann Solver: <http://www.lbmethod.org/palabos/>.

892 Legland, D., Arganda-Carreras, I., Andrey, P., 2016. MorphoLibJ: Integrated library and  
893 plugins for mathematical morphology with ImageJ. *Bioinformatics* 32, 3532–3534.  
894 <https://doi.org/10.1093/bioinformatics/btw413>

895 Malaspinas, O., Fiétier, N., Deville, M., 2010. Lattice Boltzmann method for the simulation of  
896 viscoelastic fluid flows. *J. Nonnewton. Fluid Mech.* 165, 1637–1653.  
897 <https://doi.org/10.1016/j.jnnfm.2010.09.001>

898 Mitra, S., Rodríguez de Castro, A., El Mansori, M., 2019. On the rapid manufacturing process  
899 of functional 3D printed sand molds. *J. Manuf. Process.* 42, 202–212.  
900 <https://doi.org/10.1016/j.jmapro.2019.04.034>

901 Mitra, S., Rodríguez de Castro, A., El Mansori, M., 2018. The effect of ageing process on  
902 three-point bending strength and permeability of 3D printed sand molds. *Int. J. Adv.*  
903 *Manuf. Technol.* 97, 1241–1251. <https://doi.org/10.1007/s00170-018-2024-8>

904 Ramezani Dana, H., El Mansori, M., 2019. Etude du comportement mécanique d'une  
905 structure poreuse obtenue par impression 3D au sable, in: 24ème Congrès Français de  
906 Mécanique.

907 Rodríguez de Castro, A., Agnaou, M., 2019. Numerical Investigation of the Apparent  
908 Viscosity Dependence on Darcy Velocity During the Flow of Shear-Thinning Fluids in  
909 Porous Media. *Transp. Porous Media*. <https://doi.org/10.1007/s11242-019-01279-x>

910 Sachs, E., Cima, M., Cornie, J., 1990. Three-dimensional printing: rapid tooling and  
911 prototypes directly form a CAD model. *CIRP Ann. - Manuf. Technol.* 39, 201–204.  
912 [https://doi.org/http://dx.doi.org/10.1016/S0007-8506\(07\)61035-X](https://doi.org/http://dx.doi.org/10.1016/S0007-8506(07)61035-X)

913 Schindelin, J., Arganda-Carreras, I., Frise, E., Kaynig, V., Longair, M., Pietzsch, T.,  
914 Preibisch, S., Rueden, C., Saalfeld, S., Schmid, B., Tinevez, J.Y., White, D.J.,  
915 Hartenstein, V., Eliceiri, K., Tomancak, P., Cardona, A., 2012. Fiji: An open-source  
916 platform for biological-image analysis. *Nat. Methods* 9, 676–682.  
917 <https://doi.org/10.1038/nmeth.2019>

918 Sivarupan, T., El Mansori, M., Daly, K., Mavrogordato, M.N., Pierron, F., 2018.  
919 Characterisation of 3D printed sand moulds using micro-focus X-ray computed  
920 tomography. *Rapid Prototyp. J.* <https://doi.org/10.1108/RPJ-04-2018-0091>

921 Sivarupan, T., ElMansori, M., Coniglio, N., 2017. 3D Printing Process Parameters and  
922 Properties of Additively Manufactured Sand Mold for Rapid Casting : Strength and  
923 Permeability. *Addit. Manuf.* (under review).

924 Smith, P., Reid, D.B., Environment, C., Palo, L., Alto, P., Smith, P.L., 2010. A Threshold  
925 Selection Method from Gray-Level Histograms *C*, 62–66.

926 Soulaine, C., 2015. Direct numerical simulation in fully saturated porous media. *Stanford.Edu*  
927 1–27.

928 Thabet, A., Straatman, A.G., 2018. The development and numerical modelling of a  
929 Representative Elemental Volume for packed sand. *Chem. Eng. Sci.* 187, 117–126.

930 <https://doi.org/10.1016/j.ces.2018.04.054>

931 Upadhyay, M., Sivarupan, T., El Mansori, M., 2017. 3D Printing for Rapid Sand Casting - A

932 Review. *J. Manuf. Process.* 29, 211–220. <https://doi.org/10.1016/j.jmapro.2017.07.017>

933 Xiong, Q., Baychev, T.G., Jivkov, A.P., 2016. Review of pore network modelling of porous

934 media: Experimental characterisations, network constructions and applications to

935 reactive transport. *J. Contam. Hydrol.* 192, 101–117.

936 <https://doi.org/10.1016/j.jconhyd.2016.07.002>

937

938

939

940

941

942

Accepted Manuscript